

AFIT/GAE/ENY/93D-29

AD-A273 984



A NUMERICAL DETERMINATION OF BIFURCATION
POINTS FOR LOW REYNOLDS NUMBER
CONICAL FLOWS

THESIS
Larry K. Waters
Captain, USAF

AFIT/GAE/ENY/93D-29

**S DTIC
ELECTE
DEC 17 1993
E D**

93-30639



Approved for public release; distribution unlimited

93 12 17037

PII Redacted

A NUMERICAL DETERMINATION OF BIFURCATION POINTS FOR LOW
REYNOLDS NUMBER CONICAL FLOWS

THESIS

Presented to the Faculty of the Graduate School of Engineering
of the Air Force Institute of Technology
Air University
In Partial Fulfillment of the
Requirements for the Degree of
Master of Science in Aeronautical Engineering

Larry K. Waters, B.S.
Captain, USAF

December, 1993

Accession For	
NTIS CRA&I	<input checked="" type="checkbox"/>
DTIC TAB	<input type="checkbox"/>
Unannounced	<input type="checkbox"/>
Justification	
By	
Distribution /	
Availability Codes	
Dist	Avail and/or Special
A-1	

Approved for public release; distribution unlimited

Acknowledgements

I would like to first thank my advisor, Dr. Beran, for his patience and understanding. I would also like to thank the other members of my committee, Maj Buter and Dr. King, for their support. Capt Morton deserves a special thank you. He was always willing to make time in his busy schedule to give the advise and encouragement I needed to keep going through some frustrating times. I would also like to thank my friends Doug Blake, Paul Schubert, and Bernie Frank, who were always willing to sit and listen.

The people who deserve the most gratitude are my wife Charlotte and my son Mike. As an ICU nurse, Charlotte has a job that is vastly more important than anything I do, yet she always has time to listen patiently to my problems, and give me all the support anyone could ever ask for. Mike had to endure endless excuses for why I had to spend time with my school work instead of him. Any success I have had at AFIT is directly attributable to Charlotte and Mike, my two best friends.

Larry K. Waters

Table of Contents

	Page
Acknowledgements	ii
List of Figures	vii
List of Tables	ix
Abstract	x
I. Introduction	1-1
1.1 Historical Background	1-2
1.1.1 Mach number effects	1-4
1.1.2 Geometric effects	1-4
1.2 Research Objective	1-6
II. Analysis	2-1
2.1 Model Assumptions	2-1
2.2 Linearization of Sutherland's Law	2-3
2.3 Governing Equations	2-6
2.4 Boundary Conditions	2-8
2.5 Coordinate Transformation	2-9
2.6 Discretization of the Governing Equations and Boundary Con- ditions	2-13
2.7 Implementation of Continuity at the Freestream Boundary .	2-14
2.8 Grid Generation and Discretization	2-15
2.9 Added Numerical Dissipation	2-17
III. Solution Algorithm	3-1
3.1 Newton's Method	3-1
3.2 Continuation Method	3-2

	Page
IV. Navier-Stokes Solutions	4-1
4.1 Supersonic Results	4-2
4.2 Subsonic Results	4-4
V. Conclusions and Recommendations	5-1
Bibliography	BIB-1
Appendix A. Derivation of Governing Equations	A-1
Appendix B. Derivation of Analytical Jacobian Elements	B-1
Vita	VITA-1

List of Symbols

Symbol	Definition
\bar{F}	System of nonlinear equations
$\bar{F}_{\bar{x}}$	Jacobian matrix
I	Number of nodes in the ϕ direction
J	Number of nodes in the θ direction
M	Freestream Mach number
P	Pressure
Pr	Prandtl number
R	Gas constant
Re	Reynolds number
T	Temperature
U_{∞}	Freestream velocity
V	Velocity vector
c_1, c_2	Coefficients from Sutherland's law
\hat{c}_1, \hat{c}_2	Non-dimensional coefficients from linear $\mu - e$ relationship
a_{∞}	Freestream speed of sound
d_{min}	Initial wall spacing for packed grid
e	Internal energy
f	An arbitrary variable
u	Velocity component in the radial direction
v	Velocity component in the θ direction
w	Velocity component in the ϕ direction
\bar{x}	Solution to the system of nonlinear equations
κ	Coefficient of thermal conductivity
θ_c	Cone half-angle
θ_{max}	Angle at freestream boundary
α	Angle of attack
α_{sv}	Angle of attack where symmetric vortices appear

α_{av}	Angle of attack where asymmetric vortices appear
α_{uv}	Angle of attack where unsteady vortices appear
μ	Coefficient of viscosity
ρ	Density
γ	Ratio of specific heats
λ	Second coefficient of viscosity
c_v	Specific heat at constant volume
c_p	Specific heat at constant pressure

List of Figures

Figure	Page
1.1. Mach number effects on α_{av} (12)	1-5
1.2. Possible Solution Spaces	1-6
2.1. Comparison of Sutherland's law and linearized formula	2-4
2.2. Spherical coordinate system and 2-D "plane" of constant r	2-5
2.3. Physical and Computational Domains	2-10
2.4. Nine-point Stencil for interior nodes	2-13
2.5. Stencil for one-sided boundary derivatives	2-14
2.6. Stencil for Continuity equation at freestream boundary	2-15
2.7. Node numbering in computational domain	2-17
2.8. Stencil for fourth-order dissipation	2-18
2.9. Uniform Grid	2-19
2.10. Packed Grid	2-20
3.1. Illustration of continuation procedure, Beran (4)	3-5
4.1. Supersonic Flow over Cone at $\alpha = 0$	4-7
4.2. Non-dimensional density	4-8
4.3. Non-dimensional u velocity component	4-9
4.4. Non-dimensional v velocity component	4-9
4.5. 30x81, $Re = 500, M = .3, \alpha = 5$ deg	4-10
4.6. 30x81, $Re = 500, M = .3, \alpha = 8$ deg	4-11
4.7. 30x81, $Re = 500, M = .3, \alpha = 11$ deg	4-12
4.8. 30x81, $Re = 500, M = .3, \alpha = 15$ deg	4-13
4.9. 50x81, $Re = 500, M = .3, \alpha = 5$ deg	4-14
4.10. 50x81, $Re = 500, M = .3, \alpha = 8$ deg	4-15

Figure	Page
4.11. 50x81, $Re = 500, M = .3, \alpha = 11$ deg	4-16
4.12. 50x81, $Re = 500, M = .3, \alpha = 15$ deg	4-17
4.13. 60x81, $Re = 500, M = .3, \alpha = 11$ deg	4-18
4.14. 60x81, $Re = 500, M = .3, \alpha = 15$ deg	4-19
 B.1. Nine-point Stencil for interior nodes	 B-2

List of Tables

Table		Page
2.1.	Boundary conditions for supersonic flow	2-9
2.2.	Boundary conditions for subsonic, inviscid flow	2-10
2.3.	Boundary conditions for subsonic, viscous flow	2-10
2.4.	Node relationships for nine-point stencil	2-16
4.1.	Initial boundary conditions for viscous subsonic flow	4-2
4.2.	Initial boundary conditions for inviscid subsonic flow	4-2
4.3.	Boundary conditions for subsonic, inviscid flow	4-7
4.4.	Boundary conditions for subsonic, viscous flow	4-7
4.5.	Shock angle results	4-8
4.6.	Run Conditions for Point Solutions	4-8

Abstract

It has long been established that supersonic flow over axisymmetric conical bodies at high angles of attack tend to develop a side force due to vortical asymmetry. One of the proposed reasons for the asymmetry is a bifurcation point in the solution of the Navier-Stokes equations. This study investigated the possible existence of a bifurcation point in the Navier-Stokes equations for subsonic laminar flow. Newton's method, with gauss elimination, was used to solve the steady-state, viscous, compressible Navier-Stokes equations in spherical coordinates assuming conical similarity.

A NUMERICAL DETERMINATION OF BIFURCATION POINTS FOR LOW REYNOLDS NUMBER CONICAL FLOWS

I. Introduction

Asymmetric vortices on the leeward side of slender conical bodies, such as missiles or fighter aircraft flying at high angles of attack, can result in large side forces on the body, even at zero yaw. These large side forces can have significance in vehicle directional control. The development of symmetric and asymmetric vortices on the leeward side of slender conical bodies has been observed for laminar and turbulent flows, subsonic through hypersonic speeds, and various cross-sectional shapes (13).

Experimental studies of several researchers, including (29), (30), and (38), have identified four distinct flow patterns about slender bodies at angle of attack and zero-degree sideslip. Using θ_c to denote the cone half-angle, α_{sv} the angle of attack at which symmetric vortices appear, α_{av} the angle of attack at which asymmetric vortices appear, and α_{uv} the angle of attack at which unsteady vortex shedding begins, the flow about a slender cone can be characterized by:

- 1) At low angle of attack ($0 \leq \alpha < \alpha_{sv}$), axial flow dominates and the flow is attached.
- 2) At intermediate angles of attack ($\alpha_{sv} \leq \alpha < \alpha_{av}$), a symmetric vortex pair appears on the leeward side of the body.
- 3) At higher angles of attack ($\alpha_{av} \leq \alpha < \alpha_{uv}$), crossflow dominates and the vortices become asymmetric. This results in rapidly increasing side forces, even at zero yaw.
- 4) At very high angles of attack ($\alpha_{uv} \leq \alpha < 90^\circ$), the crossflow dominates completely, resulting in an unsteady vortex shedding similar to the Karman vortex shedding typical of cylinders.

Ericsson and Reding (13), and Lowson and Ponton (23), report that for laminar flow, $\alpha_{sv} \approx \theta_c$, $\alpha_{av} \approx 2\theta_c$, and $\alpha_{uv} \approx 60^\circ$, whereas for turbulent flow $\alpha_{sv} \approx 1.3\theta_c$.

1.1 *Historical Background*

In the late 1940's, lateral instability caused by asymmetric vortices was discovered in flight tests. A great deal of experimental work followed, including Mudi et al. (25), Peake et al. (29), Stahl et al. (30), Yanta and Wardlaw (38), and Zilliac et al. (39). One of the original computational efforts was performed by Dyer et al. (11), who showed that asymmetric vortices on the leeward side of a slender cone could be predicted by standard line vortex models using symmetric boundary conditions. This study was followed up by a more detailed study by Fiddes and Smith (15), and Fiddes (14), where vortex sheets modeled by vortex filaments confirmed the earlier results. Assuming conical flow, Marconi (24) used an algorithm based on the Euler equations to further demonstrate the existence of the asymmetry in the vortex pair. In fact, Marconi found that at a critical angle of attack, α_{av} , the symmetric solution was unsteady. He observed that the only way to achieve a symmetric solution was to impose a symmetric condition.

In the late 1980's and early 1990's, more powerful computational tools brought a virtual explosion to the area of calculating asymmetric vortical flow. Researchers such as Marconi and Siclari (33), Siclari (32), Degani and Levy (9), Degani and Schiff (10), Degani (7), Kandil et al. (19), Batina (3), and Vanden and Belk (36) are but a few of the many computational efforts in this area. These studies range from subsonic to supersonic, laminar and turbulent. Complementing the computational efforts were many experimental studies, including Degani (8), Zilliac et al. (39), Modi et al. (25), Yanta and Wardlaw (38), Lawson and Ponton (23), Peake et al. (29), and Stahl et al. (34). Many of these efforts dealt with either the study of asymmetric vortices on different cross-sectional shapes, including delta wings, or the suppression of the asymmetry using fins or strakes, which impose a symmetry in the flow.

Several of the numerical solutions utilized the conical flow assumption: Batina (3), Kandil et al. (19), Siclari (32), and Siclari and Marconi (33). With the conical flow assumption, changes in the flow variables in the radial direction are neglected, so that the governing equations may be solved in two dimensions. The advantage of using this assumption is that a much more detailed numerical analysis can be performed. The disadvantage is that only inviscid, supersonic flow is truly conical, where the length scale has disap-

peared from the problem. Ericsson (12) investigated experimental results for supersonic and subsonic viscous flow and concluded that "conical flow asymmetry does indeed exist, but only up to moderate angles of attack, $\alpha < 30$ deg, where the axial flow component still has a strong influence on the crossflow-separation characteristics."

All of the results from the studies that incorporated the conical flow assumption show that asymmetric vortices develop around the critical angle $\alpha_{av} \approx 2\theta_c$. In the study performed by Siclari and Marconi (33), when starting from a symmetric initial condition the residual (difference between the exact and approximate solutions) declined by ten orders of magnitude, and at this point the solution was essentially symmetric (Category 2 above). As the iterative scheme progressed, the residual increased to almost its original value and then declined monotonically to machine zero where asymmetric vortices were observed. Monotonic convergence to an asymmetric solution could be achieved, if a small asymmetry was introduced into the initial condition. The same convergence behavior was also seen in the study by Kandil et al. (19), who used a similar algorithm. These studies utilized a time integration approach.

Other researchers, (7), (10), and (36), computed the unrestricted, three-dimensional flow, over a slender ogive-cylinder body at angle of attack. Vanden and Belk (36) computed both supersonic and subsonic flow. In both cases, a localized perturbation to the body shape was needed for the asymmetric solution (Category 3) to be stable. They report that this observation shows that vortex asymmetry at high angles of attack on slender bodies is due to a convective instability resulting from an asymmetric upstream disturbance. Degani (7) computed the subsonic laminar flow about a slender ogive-cylinder body. Solutions were obtained for angles of attack ranging from $\alpha = 20^\circ$ to $\alpha = 80^\circ$ and a Reynolds number (based on freestream conditions and cylinder diameter) of $Re_D = 200,000$. Results at a Mach number, M , of 0.2 and $\alpha = 20^\circ$ showed the flow to be steady and symmetric. The introduction of a space-invariant, time-invariant perturbation placed near the tip only made a small change to the flow structure. At $\alpha = 40^\circ$ the flow was steady and symmetric, but became asymmetric with the introduction of the perturbation. The level of the asymmetry depended on the size and location of the perturbation. When the

perturbation was removed, the flow returned to the symmetric case. These studies also used a time integration approach.

There have been several speculations as to the discrepancy between the results obtained with the conical flow assumption and those without the restriction. In regards to the results obtained by Degani and Schiff (10), where asymmetric vortices only appeared when a perturbation was introduced into the flow, Kandil et al. (19) report that the reason for this is the result of "the smallest scale of the grid at the solid boundary and the damping effect of the numerical dissipation in the axial direction, in addition to the grid-fineness distribution." Vanden and Belk (36) claim that the approximate factorization in the numerical scheme used by Siclari (32) introduced an error into the transient solution.

Complicating the comparative analysis is the inability to achieve a perfectly symmetric test in experimental work. If the asymmetry is caused by arbitrarily small perturbations present near the nose tip of the model, then the asymmetry will be observed experimentally, especially since machining processes used to construct the test models are not perfect, and small surface imperfections will always exist. It is these imperfections, which can be large compared to the model radius near the model tip, that could be responsible for flow asymmetry.

1.1.1 Mach number effects. Several researchers, including (19), (12), (20), and (13) have investigated the effect of Mach number on the angle of attack at which the asymmetry appears and the relative strength of the vortices. Their conclusion is that as Mach number increases, α_{av} increases, while α_{sv} is not affected. This trend can be seen in Figure 1.1, from (12). Also, the relative strength of the side forces is greater at subsonic speeds.

1.1.2 Geometric effects. Again, several researchers, (23), (38), (20), (32), and (13), have studied the effect of different cross-sectional shapes, blunt versus sharp noses, and different fineness ratios of bodies. The cumulative results indicate that as the body becomes thinner (more elliptic), it becomes more resistant to the onset of the asymmetry.

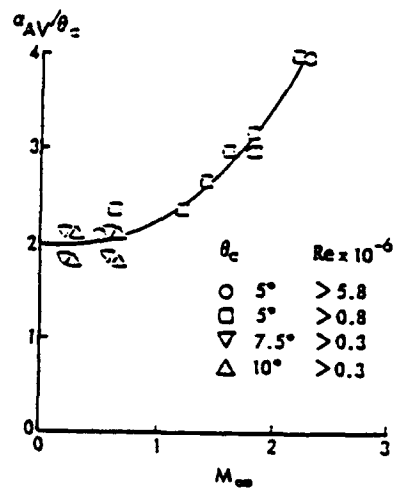


Figure 1.1 Mach number effects on α_{av} (12)

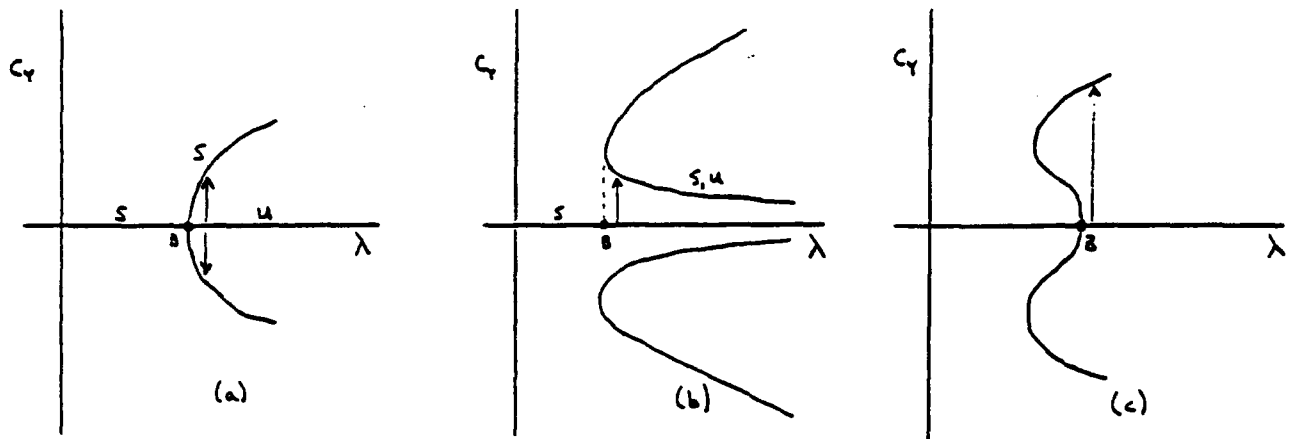


Figure 1.2 Possible Solution Spaces

Siclari found that asymmetric vortices develop for cross-sectional shapes other than circular cones. His study included elliptic, biparabolic, and biwedge cross-sections.

Much lower side forces have been noted for blunt versus sharp nosed bodies. This is possibly due to the fact that a bump near the nose, caused by surface roughness, has greater impact on the sharp nose.

1.2 Research Objective

The main objective of this study is to evaluate the solution space available to the Navier-Stokes equations, assuming conical similarity, for flows around a slender, circular cones at angle of attack. A direct numerical procedure is used to compute bifurcation points in the solution space. At such points, symmetric vortex structures become unstable, while stable asymmetric vortex structures become admissible. Most of the previous investigations in this area have dealt with the supersonic flow regime. This study provides additional results for subsonic flow.

Figure 1.2 shows three possible solution spaces available for the Navier-Stokes equations. The first picture (a) represents the most likely solution space, and the one presented by Siclari and Marconi (33). In these figures, the ordinate label is λ , which represents a free parameter in the solution. For this analysis, the free parameter is $\lambda = \alpha/\theta c$. The abscissa represents a measurable quantity that changes after the bifurcation point is passed. For this analysis, the side force coefficient is an applicable parameter. The trivial path is designated as the path where the side force coefficient is zero. The point B represents the bifurcation point. To the left of B, the trivial path is the only solution available, and is considered stable (s). To the right of B, the trivial path becomes an unstable solution (u), and the pitchfork path represents the stable solution. There are two acceptable solution paths, one above the ordinate and one below. These solutions are identical, mirror images of each other. For this analysis, the two solutions represent which side of the cone the asymmetry occurs on. The reason Newton's method with gauss elimination was chosen as the solution technique for this study is because this combination, coupled with the continuation method, allows for the systematic computation of the entire solution space, including the unstable branches. Time integration techniques, used by other researchers, can not be efficiently coupled with a continuation method. Also, considering the convergence behavior experienced by Siclari and Marconi (33), time integration routines could result in different solutions of the computed flowfield, depending on the convergence criteria used.

II. Analysis

In this Chapter, a model problem is formulated for the investigation of low-speed, conical flows, including equations of motion, boundary conditions, and discretization. The implications and validity of the assumptions of the model formulation are covered in Section 2.1. Sutherland's law, used to model the coefficient of viscosity, is simplified through linearization, described in Section 2.2. The non-dimensional governing equations, derived in Appendix A, are presented in Section 2.3, while boundary conditions are described in Section 2.4. The coordinate transformation from physical to computational space is outlined in Section 2.5. Spatial discretization of the physical domain is covered in Section 2.6. The approximation of the derivative terms in the governing equations and the boundary conditions is shown in Section 2.7. The methodology for adding fourth-order numerical dissipation is presented in Section 2.8.

2.1 Model Assumptions

The assumptions used in the analysis are:

- Steady flow
- Laminar flow
- Conical flow
- Thermally and calorically perfect gas
- Constant ratio of specific heats
- Linearized form of Sutherland's law
- Constant Prandtl number
- Stokes' hypothesis
- Adiabatic wall
- Normal pressure gradient at wall is zero

Steady flow implies $\frac{\partial f}{\partial t} = 0$. In this context, and throughout the remainder of this chapter, f represents any one of the five unknown variables in the problem: density, ρ , the

three velocity components, u , v , and w , and internal energy, e . Assuming a calorically and thermally perfect gas, implies

$$P = \rho RT \quad e = c_v T. \quad (2.1)$$

The ratio of specific heats, γ , is assumed to be 1.4. The assumption of Stokes' hypothesis means that the bulk viscosity is zero, so the second coefficient of viscosity, λ , is given by $\lambda = -\frac{2}{3}\mu$.

The adiabatic wall assumption implies that the derivative of the temperature at the wall is zero. Linearizing Sutherland's law implies a small variation in the non-dimensional temperature throughout the flowfield. Figure 2.1 shows the comparison of Sutherland's law and the linearized formula, derived in Section 2.2. Comparing the non-dimensional viscosity given by Sutherland's law (2.3) and the linearized formula (2.10) gives a difference of 2.99% for $M = 0.3$ and 2.93% for $M = 0.7$.

With conical similarity, changes in the flow variables occurring along rays (in the r direction) emanating from the cone apex are assumed to vanish. As shown in Figure 2.2, r is one of the three coordinate directions for a spherical coordinate system. Peake and Tobak (30) illustrate conical flow by stating that "stream surfaces projected on to concentric spheres centered at the apex (called conical flow streamlines) are then similar." The implications are that all derivatives with respect to r of the flow variables, ρ , u , v , w , and e vanish.

Conical similarity is exact for supersonic, inviscid flow since there is no length scale in the problem. For supersonic, viscous flow, the flow is not exactly conical, because in the boundary layer the flow is subsonic. According to (30), a laminar boundary layer is not exactly conical, because the boundary layer grows as $r^{0.5}$, and in a fully turbulent boundary layer, where the boundary layer grows as r , the flow is nearly conical. Peake and Tobak (30) summarize the issue of conical flow by stating:

When the Reynolds number is sufficiently high so that transition occurs in proximity to the apex, the near-conical nature of the experimentally measured flow demonstrates a virtual absence of length effects in the streamwise direction: the flow is dominated completely by the circumferential pressure field.

Thus, the characteristics of these flow fields can be determined through measurement or by computation at essentially one streamwise station. In fully turbulent and fully laminar subsonic freestream flow, even though base and thickness effects become measurable, the circumferential pressure gradients still dominate, to the extent that virtual conicity of the separation lines and shear-stress directions are still maintained.

The applicability of the conical flow assumption for subsonic flows is the subject of a paper by Ericsson (12). In this paper Ericsson reviewed experimental results and concluded that "conical flow asymmetry does exist on very slender cones because of the still-present strong axial flow component at $2\theta_c < \alpha < 30^\circ$." On cones where the asymmetry does not develop until $\alpha > 30^\circ$, the flow is nonconical. For this reason, the cone half-angle used in this study is $\theta_c = 5$ degrees.

The assumptions of a thermally and calorically perfect gas, along with constant ratio of specific heats, is valid for the subsonic and low supersonic flows investigated in this study (2). Reference (37) supports the assumption of constant Pr and zero pressure gradient normal to the wall in the boundary layer. Symmetric and asymmetric vortices have been shown to exist in flows over circular cones for steady, laminar flow (References (13), (19), (33), (7)). No attempt was made to model turbulent flows.

2.2 Linearization of Sutherland's Law

Since viscosity is not assumed to be a constant, a relationship is desired that expresses viscosity in terms of one or more of the unknown variables. Sutherland's law (1) provides this relationship:

$$\mu(T) = \frac{c_1 T^{3/2}}{c_2 + T}, \quad (2.2)$$

where $c_2 = 110.4^\circ K$ and c_1 will be eliminated through non-dimensionalization. Using (2.1), μ can be expressed as a function of the internal energy, e . However, with this expression, the complexity of the derivation of analytical Jacobian elements is greatly increased. (examples of the derivation of Jacobian elements appear in Appendix B). To avoid such complexity, (2.2) is first placed in non-dimensional form and then linearized to provide a simpler expression for μ .

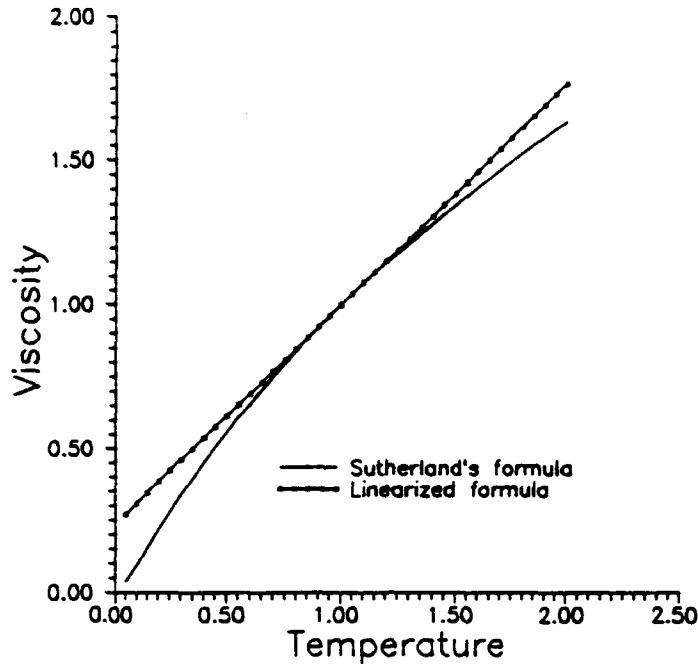


Figure 2.1 Comparison of Sutherland's law and linearized formula

The freestream viscosity is found by evaluating (2.2) at the freestream temperature, T_∞ . The appropriate non-dimensional scale factors for μ and T are then the freestream values, μ_∞ and T_∞ (all of the non-dimensional scale factors are given in Appendix A). Using the superscript (*) to denote a non-dimensional value, equation (2.2) is written in non-dimensional form as

$$\mu^* = \frac{\mu(T)}{\mu(T_\infty)} = \frac{c_1 T^{3/2} (c_2 + T_\infty)}{(c_2 + T) c_1 T_\infty^{3/2}} = \left(\frac{T}{T_\infty}\right)^{3/2} \frac{c_2/T_\infty + 1}{c_2/T_\infty + T/T_\infty}. \quad (2.3)$$

Using $T^* = T/T_\infty$ and $c_2^* = c_2/T_\infty$, (2.3) is rewritten as

$$\mu^*(T^*) = (T^*)^{3/2} \left(\frac{c_2^* + 1}{c_2^* + T^*} \right). \quad (2.4)$$

Equation (2.4) is linearized by expanding it in a first-order Taylor series expansion about T_∞^* :

$$\mu^* = \mu^*(T_\infty^*) + \left. \frac{\partial \mu^*}{\partial T^*} \right|_{T_\infty^*} \Delta T^* + O(\Delta T^*)^2. \quad (2.5)$$

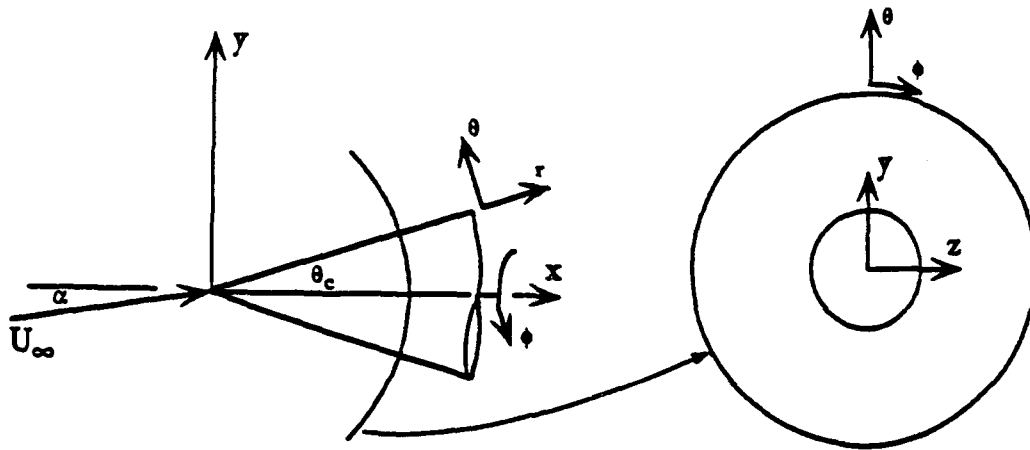


Figure 2.2 Spherical coordinate system and 2-D "plane" of constant r

Differentiating equation (2.4) with respect to T^* gives

$$\frac{\partial \mu^*}{\partial T^*} = \frac{(c_2^* + 1)}{(c_2^* + T^*)^2} \left[\frac{3}{2}(T^*)^{1/2}(c_2^* + T^*) - (T^*)^{3/2} \right], \quad (2.6)$$

$$\left. \frac{\partial \mu^*}{\partial T^*} \right|_{T_\infty^*} = \left[\frac{3}{2} - \frac{1}{(c_2^* + 1)} \right]. \quad (2.7)$$

Substituting (2.7) into (2.5), along with $\Delta T^* = T^* - T_\infty^* = T^* - 1$, gives

$$\mu^*(T^*) = \left[\frac{3}{2} - \frac{1}{c_2^* + 1} \right] (T^* - 1) + 1. \quad (2.8)$$

Now, T^* is replaced with e^* , one of the unknown non-dimensional variables, using

$$e = c_v T = \frac{RT}{(\gamma - 1)}.$$

where e and T are non-dimensionalized using the scale factors provided in Appendix A, resulting in

$$U_{\infty}^2 e^* = \frac{RT^*T_{\infty}}{(\gamma - 1)} \Rightarrow T^* = \gamma(\gamma - 1)M^2 e^*. \quad (2.9)$$

Substituting (2.9) into (2.8) results in a linear, non-dimensional form of μ in terms of the internal energy:

$$\mu^* = \hat{c}_1 e^* + \hat{c}_2, \quad (2.10)$$

where \hat{c}_1 and \hat{c}_2 are given by:

$$\hat{c}_1 = \left[\frac{3}{2} - \frac{1}{c_2^* + 1} \right] \gamma(\gamma - 1)M^2, \quad \hat{c}_2 = 1 - \left[\frac{3}{2} - \frac{1}{c_2^* + 1} \right]. \quad (2.11)$$

The thermal conductivity, κ , is related to μ through the assumption of a constant Prandtl number, Pr , where

$$Pr \equiv \frac{c_p \mu}{\kappa}. \quad (2.12)$$

Non-dimensionalization of (2.12) yields

$$Pr = \frac{c_p \mu^* \mu_{\infty}}{\kappa^* \kappa_{\infty}} \Rightarrow Pr = \frac{\mu^*}{\kappa^*} Pr. \quad (2.13)$$

When $Pr = \text{constant}$, (2.13) provides

$$\mu^* = \kappa^*. \quad (2.14)$$

Equation (2.10) is used to replace the non-dimensional thermal conductivity, κ^* , which appears in the energy equation (derived in Appendix A) For the remainder of the analysis, the superscript (*), representing a non-dimensional variable, is dropped for convenience.

2.3 Governing Equations

Following the assumptions outlined in Sections 2.1 and 2.2, the non-dimensional governing equations are developed in Appendix A. A schematic of the spherical coordinate system is given in Figure 2.2. With the subscripts θ and ϕ denoting differentiation, the

non-dimensional governing equations in spherical coordinates are:

Continuity equation

$$2\rho u \sin\theta + \rho v \cos\theta + v\rho_\theta \sin\theta + \rho v_\theta \sin\theta + \rho w_\phi + w\rho_\phi = 0 \quad (2.15)$$

r-momentum equation

$$\begin{aligned} \rho r \left[vu_\theta + \frac{wu_\phi}{\sin\theta} - v^2 - w^2 \right] + \frac{\hat{c}_1 e_\theta}{Re} [v - u_\theta] + \frac{\hat{c}_1 e_\phi}{Re} \left[\frac{w}{\sin\theta} - \frac{u_\phi}{\sin^2\theta} \right] \\ + \frac{\hat{c}_1 e + \hat{c}_2}{Re} \left[\frac{8u}{3} + \frac{7v \cot\theta}{3} + \frac{7v_\theta}{3} + \frac{7w_\phi}{3 \sin\theta} - u_{\theta\theta} - \frac{u_{\phi\phi}}{\sin^2\theta} - u_\theta \cot\theta \right] = 0 \end{aligned} \quad (2.16)$$

\theta-momentum equation

$$\begin{aligned} \rho r \left[vv_\theta + \frac{vw_\phi}{\sin\theta} + uv - w^2 \cot\theta \right] + r(\gamma - 1) [\rho e_\theta + e\rho_\theta] \\ + \frac{\hat{c}_1 e_\theta}{Re} \left[\frac{2v \cot\theta}{3} + \frac{2w_\phi}{3 \sin\theta} - \frac{4v_\theta}{3} - \frac{2u}{3} \right] + \frac{\hat{c}_1 e_\phi}{Re} \left[\frac{w \cos\theta}{\sin^2\theta} - \frac{w_\theta}{\sin\theta} - \frac{v_\phi}{\sin^2\theta} \right] \\ + \frac{\hat{c}_1 e + \hat{c}_2}{Re} \left[2v + \frac{7w_\phi \cos\theta}{3 \sin^2\theta} + 2v \cot^2\theta - \frac{4v_{\theta\theta}}{3} - \frac{v_{\phi\phi}}{\sin^2\theta} \right. \\ \left. - \frac{w_{\theta\phi}}{3 \sin\theta} - \frac{8u_\theta}{3} - \frac{4v_\theta \cot\theta}{3} - \frac{2v}{3 \sin^2\theta} \right] = 0 \end{aligned} \quad (2.17)$$

\phi-momentum equation

$$\begin{aligned} \rho r \left[vw_\theta + \frac{ww_\phi}{\sin\theta} + wu + vw \cot\theta \right] + \frac{r(\gamma - 1)}{\sin\theta} [e\rho_\phi + \rho e_\phi] \\ - \frac{\hat{c}_1 e_\theta}{Re} \left[w_\theta - w \cot\theta + \frac{v_\phi}{\sin\theta} \right] - \frac{\hat{c}_1 e_\phi}{Re} \left[\frac{4w_\phi}{3 \sin^2\theta} + \frac{2u}{3 \sin\theta} + \frac{4v \cos\theta}{3 \sin^2\theta} - \frac{2v_\theta}{3 \sin\theta} \right] \\ - \frac{\hat{c}_1 e + \hat{c}_2}{Re} \left[\frac{4w_{\phi\phi}}{3 \sin^2\theta} + w_{\theta\theta} + \frac{v_{\theta\phi}}{3 \sin\theta} + \frac{8u_\phi}{3 \sin\theta} + \frac{7v_\phi \cos\theta}{3 \sin^2\theta} \right. \\ \left. - 2w + \frac{w}{\sin^2\theta} + w_\theta \cot\theta - 2w \cot^2\theta \right] = 0 \end{aligned} \quad (2.18)$$

Energy equation

$$\rho r \left[ve_\theta + \frac{we_\phi}{\sin\theta} \right] + (\gamma - 1) r e \rho \left[2u + v \cot\theta + v_\theta + \frac{w_\phi}{\sin\theta} \right]$$

$$\begin{aligned}
& - \frac{\gamma(\hat{c}_1 e + \hat{c}_2)}{Pr Re} \left[e_\theta \cot\theta + e_{\theta\theta} + \frac{e_{\phi\phi}}{\sin^2\theta} \right] - \frac{\gamma\hat{c}_1}{Pr Re} \left[e_\theta^2 + \frac{e_\phi^2}{\sin^2\theta} \right] \\
& - \frac{\hat{c}_1 e + \hat{c}_2}{Re} \left[\frac{4v_\theta^2}{3} + \frac{4uv_\theta}{3} + \frac{4u^2}{3} + \frac{4w_\phi^2}{3\sin^2\theta} + \frac{4v^2 \cot^2\theta}{3} \right. \\
& + \frac{4uw_\phi}{3\sin\theta} + \frac{8vw_\phi \cot\theta}{3\sin\theta} + \frac{4uv \cot\theta}{3} + \frac{v_\phi^2}{\sin^2\theta} + w_\theta^2 + w^2 \cot^2\theta \\
& + \frac{2w_\theta v_\phi}{\sin\theta} - \frac{2wv_\phi \cot\theta}{\sin\theta} - 2ww_\theta \cot\theta + \frac{u_\phi^2}{\sin^2\theta} - \frac{2wu_\phi}{\sin\theta} \\
& \left. + w^2 + v^2 + u_\theta^2 - 2vu_\theta - \frac{4v_\theta w_\phi}{3\sin\theta} - \frac{4vv_\theta \cot\theta}{3} \right] = 0 \tag{2.19}
\end{aligned}$$

2.4 Boundary Conditions

The governing equations are solved at all the internal nodes, therefore only two physical surfaces require boundary conditions. These surfaces are shown in Figure 2.2, where the inner circle represents the wall boundary, and the outer circle represents the freestream boundary. For the wall, the pressure derivative normal to the wall is set equal to zero, and an adiabatic wall condition is used for all the runs. This implies,

$$\frac{\partial P}{\partial n} = 0 \tag{2.20}$$

$$\frac{\partial T}{\partial n} = 0 \tag{2.21}$$

These boundary conditions are used in all the other computational efforts in this area (7), (10), (19), (32), (33), and (36). The normal pressure derivative can be considered a first step approximation, where a more accurate boundary condition would be setting normal momentum equal to zero. Using equation (A.12), which relates pressure to density and internal energy using the perfect gas assumptions, along with equation (2.9), which relates temperature to internal energy, equations (2.20 - 2.21) can be expressed as

$$\frac{\partial \rho}{\partial n} = 0 \tag{2.22}$$

$$\frac{\partial e}{\partial n} = 0 \tag{2.23}$$

Wall	Freestream Boundary
$\frac{\partial \rho}{\partial n} = 0$	$\rho = 1$
$\frac{\partial u}{\partial n} = 0$	$u = u_{fs}$
$v = 0$	$v = v_{fs}$
$w = 0$	$w = 0$
$\frac{\partial e}{\partial n} = 0$	$e = e_{fs}$

Table 2.1 Boundary conditions for supersonic flow

For the viscous flow cases, no slip at the wall is enforced: $u = v = w = 0$. For the inviscid flow cases, slip flow and impermeability give $\frac{\partial u}{\partial n} = 0$, $\frac{\partial w}{\partial n} = 0$, and $v = 0$.

On the freestream boundary (denoted by the subscript fs), a general set of equations is used to determine the values for the flow velocities in terms of the angle of attack, α , and the coordinate angles, θ and ϕ :

$$u_1 = \cos \alpha \cos \theta \quad u_2 = \sin \alpha \sin \theta \cos \phi \quad u_{fs} = (u_1^2 + u_2^2)^{1/2} \quad (2.24)$$

$$v_1 = -\cos \alpha \sin \theta \quad v_2 = \sin \alpha \cos \theta \cos \phi \quad v_{fs} = (v_1^2 + v_2^2)^{1/2} \quad (2.25)$$

$$w_1 = 0 \quad w_2 = -\sin \alpha \sin \phi \quad w_{fs} = (w_1^2 + w_2^2)^{1/2} \quad (2.26)$$

Equations (2.24 - 2.26) are also used to initialize the flow velocities.

An expression for non-dimensional internal energy at the freestream boundary, e_{fs}^* , is obtained by evaluating equation (2.9) at $T_{fs}^* = 1$. Therefore (dropping the (*) for convenience),

$$e_{fs} = \frac{1}{\gamma(\gamma - 1)M^2}. \quad (2.27)$$

The boundary conditions for each case are summarized in Tables (2.1 - 2.3). For subsonic flow, the continuity equation is used as a freestream boundary condition. Section 2.6 outlines the use of the continuity as a boundary condition.

2.5 Coordinate Transformation

In computational fluid dynamics, the governing equations and boundary conditions are solved at a finite number of discrete points which represent the solution domain. In

Wall	Freestream Boundary
$\frac{\partial p}{\partial n} = 0$	continuity
$\frac{\partial u}{\partial n} = 0$	$u^2 + v^2 + w^2 = 1$
$v = 0$	$\rho = 1$
$\frac{\partial w}{\partial n} = 0$	$w = w_{fs}$
$\frac{\partial e}{\partial n} = 0$	$e = e_{fs}$

Table 2.2 Boundary conditions for subsonic, inviscid flow

Wall	Freestream Boundary
$\frac{\partial p}{\partial n} = 0$	continuity
$u = 0$	$u^2 + v^2 + w^2 = 1$
$v = 0$	$\rho = 1$
$w = 0$	$w = w_{fs}$
$\frac{\partial e}{\partial n} = 0$	$e = e_{fs}$

Table 2.3 Boundary conditions for subsonic, viscous flow

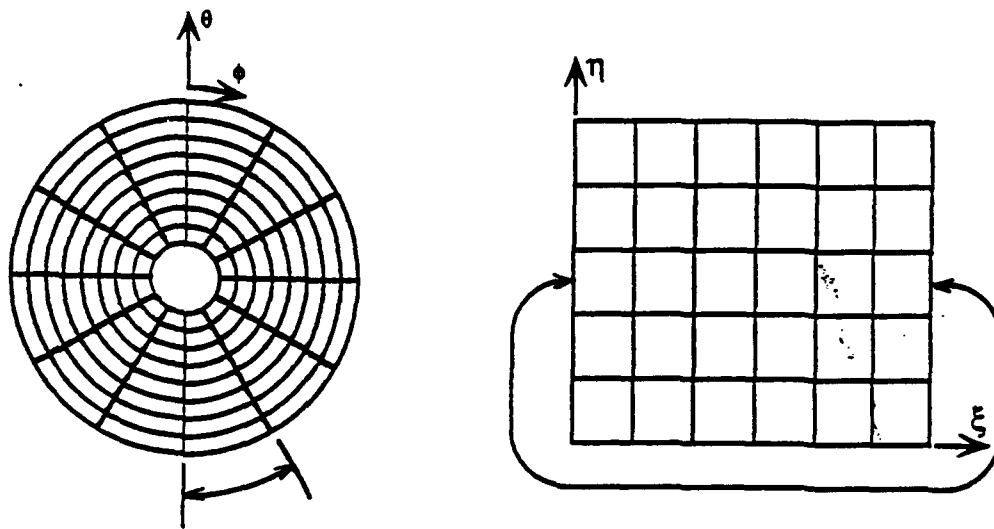


Figure 2.3 Physical and Computational Domains

the physical (ϕ, θ) space, grid points need to be clustered near the wall so the boundary layer can be properly resolved. This can be achieved by either uneven spacing between grid points in the radial direction, or by placing many more evenly spaced points along each radial line. Clearly the first approach is more efficient computationally. However, the standard second-order-accurate difference approximations used in the discretization of the governing equations require a uniform spacing between nodes. Even spacing is obtained, with node clustering in the physical domain, through a coordinate transformation of the physical domain to a *computational* domain. In this problem, the physical space is designated by the coordinate pair (ϕ, θ) , and the computational space is designated by the coordinate pair (ξ, η) , where Figure 2.3 shows the mapping between the two domains. For this study, the physical domain could be separated anywhere, but the windward side of the cone was selected because the gradients in the dependent variables are smaller in this region. Using subscripts to denote differentiation, the transformation, from (16), is expressed in general terms as

$$\phi = \phi(\xi, \eta), \quad \theta = \theta(\xi, \eta), \quad (2.28)$$

which, from the chain rule of partial differentiation, leads to

$$d\phi = \phi_\xi d\xi + \phi_\eta d\eta, \quad d\theta = \theta_\xi d\xi + \theta_\eta d\eta. \quad (2.29)$$

Similarly, the reverse transformation yields

$$\xi = \xi(\phi, \theta), \quad \eta = \eta(\phi, \theta), \quad (2.30)$$

$$d\xi = \xi_\phi d\phi + \xi_\theta d\theta, \quad d\eta = \eta_\phi d\phi + \eta_\theta d\theta. \quad (2.31)$$

When expressed in matrix form, the transformation is

$$\begin{bmatrix} \xi_\phi & \xi_\theta \\ \eta_\phi & \eta_\theta \end{bmatrix} = \begin{bmatrix} \phi_\xi & \phi_\eta \\ \theta_\xi & \theta_\eta \end{bmatrix}^{-1} = \frac{1}{J} \begin{bmatrix} \theta_\eta & -\phi_\eta \\ -\theta_\xi & \phi_\xi \end{bmatrix},$$

where the Jacobian is defined as

$$J = \phi_\xi \theta_\eta - \phi_\eta \theta_\xi.$$

The metrics of the transformation are

$$\xi_\phi = \frac{\theta_\eta}{J} \quad \xi_\theta = -\frac{\phi_\eta}{J} \quad \eta_\phi = -\frac{\theta_\xi}{J} \quad \eta_\theta = \frac{\phi_\xi}{J}.$$

The metrics and the Jacobian are evaluated numerically at all node points in the domain using the difference approximations provided in Section 2.7.

The spatial derivatives are transformed from physical to computational space with the following formulas, from (16) and (35),

$$f_\phi = \xi_\phi f_\xi + \eta_\phi f_\eta, \quad f_\theta = \xi_\theta f_\xi + \eta_\theta f_\eta, \quad (2.32)$$

$$\begin{aligned} f_{\phi\phi} &= \xi_\phi^2 f_{\xi\xi} + 2\xi_\phi\eta_\phi f_{\xi\eta} + \eta_\phi^2 f_{\eta\eta} \\ &\quad - (\xi_\phi^2 \theta_{\xi\xi} + 2\xi_\phi\eta_\phi \theta_{\xi\eta} + \eta_\phi^2 \theta_{\eta\eta})(\xi_\phi f_\xi + \eta_\phi f_\eta) \\ &\quad - (\xi_\phi^2 \phi_{\xi\xi} + 2\xi_\phi\eta_\phi \phi_{\xi\eta} + \eta_\phi^2 \phi_{\eta\eta})(\xi_\phi f_\xi + \eta_\phi f_\eta), \end{aligned} \quad (2.33)$$

$$\begin{aligned} f_{\theta\theta} &= \xi_\theta^2 f_{\xi\xi} + 2\xi_\theta\eta_\theta f_{\xi\eta} + \eta_\theta^2 f_{\eta\eta} \\ &\quad - (\xi_\theta^2 \theta_{\xi\xi} + 2\xi_\theta\eta_\theta \theta_{\xi\eta} + \eta_\theta^2 \theta_{\eta\eta})(\xi_\theta f_\xi + \eta_\theta f_\eta) \\ &\quad - (\xi_\theta^2 \phi_{\xi\xi} + 2\xi_\theta\eta_\theta \phi_{\xi\eta} + \eta_\theta^2 \phi_{\eta\eta})(\xi_\theta f_\xi + \eta_\theta f_\eta), \end{aligned} \quad (2.34)$$

$$\begin{aligned} f_{\theta\phi} &= \xi_\theta \xi_\phi f_{\xi\xi} + (\eta_\theta \xi_\phi + \xi_\theta \eta_\phi) f_{\xi\eta} + \eta_\phi \eta_\theta f_{\eta\eta} \\ &\quad + (\eta_\theta \theta_{\eta\eta} + \xi_\theta \theta_{\xi\eta} - \xi_\theta \xi_\phi J_\xi - \eta_\theta \xi_\phi J_\eta) \frac{f_\xi}{J} \\ &\quad - (\xi_\theta \theta_{\xi\xi} + \eta_\theta \theta_{\xi\eta} + \eta_\theta \eta_\phi J_\eta + \xi_\theta \eta_\phi J_\xi) \frac{f_\eta}{J}, \end{aligned} \quad (2.35)$$

$$\frac{J_\xi}{J} = \xi_\phi \phi_{\xi\xi} + \eta_\theta \theta_{\xi\eta} + \eta_\phi \phi_{\xi\eta} + \xi_\theta \theta_{\xi\xi}, \quad (2.36)$$

$$\frac{J_\eta}{J} = \xi_\phi \phi_{\xi\eta} + \eta_\theta \theta_{\eta\eta} + \eta_\phi \phi_{\eta\eta} + \xi_\theta \theta_{\xi\eta}. \quad (2.37)$$

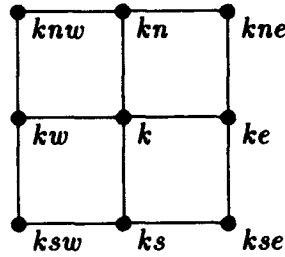


Figure 2.4 Nine-point Stencil for interior nodes

2.6 Discretization of the Governing Equations and Boundary Conditions

Following the transformation of the governing equations to the (ξ, η) computational space, the spatial derivatives are approximated to second-order-accuracy with discrete central-difference formulas. First and second derivatives of ξ and η , as well as cross-derivative terms, appear in the transformed equations. Application of central-difference formulas at a given node, k , requires information from adjacent node points. For the central-difference formulas required in this study, the *influential neighbors* of an interior node point are contained within a nine-point *computational stencil*, shown in Figure 2.4.

The difference approximations, from (1), used for the interior nodes, are

$$f_{\xi}|_k = \frac{f_{ke} - f_{kw}}{2\Delta\xi}, \quad (2.38)$$

$$f_{\eta}|_k = \frac{f_{kn} - f_{ks}}{2\Delta\eta}, \quad (2.39)$$

$$f_{\xi\xi}|_k = \frac{f_{ke} - 2f_k + f_{kw}}{\Delta\xi}, \quad (2.40)$$

$$f_{\eta\eta}|_k = \frac{f_{kn} - 2f_k + f_{ks}}{\Delta\eta}, \quad (2.41)$$

$$f_{\xi\eta}|_k = \frac{1}{2\Delta\xi} \left(\frac{f_{kne} - f_{kse}}{2\Delta\eta} - \frac{f_{knw} - f_{ksw}}{2\Delta\eta} \right). \quad (2.42)$$

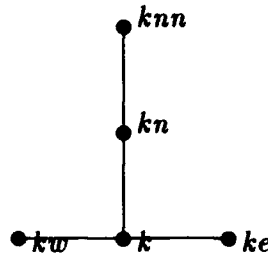


Figure 2.5 Stencil for one-sided boundary derivatives

For the wall boundary nodes, normal derivatives are replaced directly with η derivative terms. One-sided, second-order-accurate difference approximations are used to approximate the η derivatives:

$$f_{\eta} = \frac{-3f_k + 4f_{kn} - f_{knn}}{2\Delta\xi}, \quad (2.43)$$

where Figure 2.5 shows the stencil used for the one-sided differences needed for the boundary derivatives. A square node arrangement is used for all cases, so $\Delta\xi = \Delta\eta = 1$.

2.7 Implementation of Continuity at the Freestream Boundary

For subsonic flow, the continuity equation (2.15) is used as a freestream boundary condition. This equation is written as

$$2\rho u \sin\theta + (\rho v \sin\theta)_{\theta} + (\rho w)_{\phi} = 0 \quad (2.44)$$

The equation is rewritten in this form so that the first and second terms can be evaluated at the midpoint between the boundary node and the next node in from the boundary, shown in Figure 2.6. The difference approximation (2.36) is used to represent the ξ derivative term. The first term is represented by averaging the values at the midpoint.

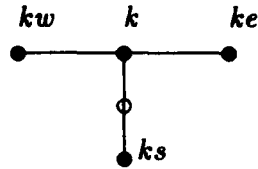


Figure 2.6 Stencil for Continuity equation at freestream boundary

A second-order-accurate difference about the midpoint is used to represent the η derivative term, so only two node points are required. The approximation equation is

$$f_{\eta} = \frac{f_k - f_{ks}}{\Delta\eta}. \quad (2.45)$$

All of the grids used in the study have evenly spaced radial lines around the cone, covered more extensively in section 2.7. This results in the metrics, ξ_{θ} and η_{ϕ} , being zero. Therefore the continuity equation used for the freestream boundary equation is

$$\begin{aligned} &(\rho u \sin\theta)_k + (\rho u \sin\theta)_{ks} + \eta_{\theta} [(\rho v \sin\theta)_k - (\rho v \sin\theta)_{ks}] \\ &+ \frac{\xi_{\phi}}{2} [(\rho w)_{ke} - (\rho w)_{kw}] = 0. \end{aligned} \quad (2.46)$$

2.8 Grid Generation and Discretization

Two different grids are used in the analysis. The first is used for the inviscid cases, both supersonic and subsonic. For these cases, there is no boundary layer to resolve so there is no need to cluster the points near the cone surface. Therefore, the radial lines are evenly spaced around the cone, and the points are evenly spaced along each radial line. When the flow is viscous and subsonic, node points must be clustered near the cone surface to accurately resolve the boundary layer. The radial lines are still spaced evenly around the cone, but the nodes along each radial line are distributed using a geometric progression, outlined in (6). Figures (2.9) and (2.10) show examples of the different grids.

The nodes in the computational domain are numbered using a row-by-row convention, as shown in Figure 2.7. The advantage of numbering the nodes this way, as compared to

Node	$i = 1$	$i = I$	$2 \leq i \leq I - 1$
ke	$k + 1$	$k - I + 1$	$k + 1$
kw	$k + I - 1$	$k - 1$	$k - 1$
kn	$k + I$	$k + I$	$k + I$
ks	$k - I$	$k - I$	$k - I$
kne	$k + I + 1$	$k + 1$	$k + I + 1$
knw	$k + 2I - 1$	$k + I - 1$	$k + I - 1$
kse	$k - I + 1$	$k - 2I + 1$	$k - I + 1$
ksw	$k - 1$	$k - I + 1$	$k - I - 1$

Table 2.4 Node relationships for nine-point stencil

column-by-column, is that the governing equations could be used with the standard nine-point stencil, shown in Figure 2.4, at the nodes adjacent to the separation region, shown in Figure (2.3). If the nodes are numbered in a column-by-column scheme, then boundary equations would be necessary for the nodes bordering the separation region. An example of this is the two-dimensional flow over a circular cylinder, where the grid is typically cut on the windward (upstream) side of the cylinder and symmetry boundary conditions are used for the node points at the cut. This situation is avoided in this study, because symmetry boundary conditions may affect the development of asymmetric vortices. The disadvantage of row-by-row numbering is the bandwidth of the Jacobian matrix is directly related to the second-order-accurate difference approximations used to approximate the wall derivative boundary conditions, and cross-derivative terms in the momentum equations.

Letting i represent the radial line, and j represent the node on a radial line, starting with 1 at the wall, the node number k is found by

$$k = (j - 1) * I + i. \quad (2.47)$$

Table 2.8 describes the relationship between the primary node k and the nodes in the nine-point stencil at different radial lines in the domain.

As can be seen from Table 2.8, the bandwidth caused by numbering the nodes using a row-by-row scheme is $4I+1$ due to using second-order accurate one-sided differences to represent the wall boundary conditions. The maximum bandwidth needed for the separation nodes ($i = 1, i = I$) is $4I-1$. The computational speed for the solution algorithm,

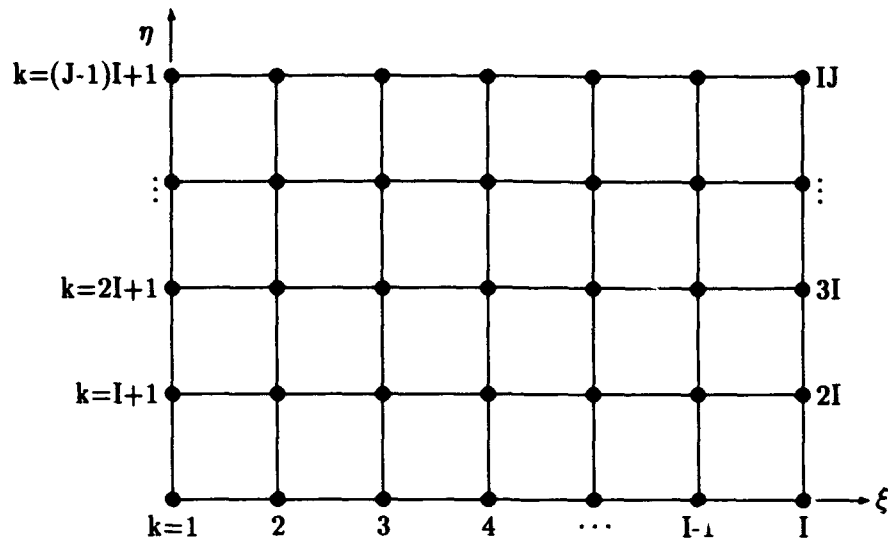


Figure 2.7 Node numbering in computational domain

outlined in Chapter III, is largely determined by the bandwidth of the Jacobian matrix. As the bandwidth is increased, the time required for convergence increases exponentially.

2.9 Added Numerical Dissipation

For the subsonic, viscous flow cases, fourth-order numerical dissipation is added to provide numerical smoothing. This smoothing diminishes the very small oscillations in the computed flow variables present in the solutions near the freestream boundary, caused by a lack of grid resolution. The added dissipation also affects the numerical results near the body, so care must be taken when determining the amount of extra dissipation added. Figure 2.8 shows the stencil needed for the added dissipation. The difference approximations, from (1), for fourth-order spatial derivatives are

$$\frac{\partial^4 f}{\partial \xi^4} = \frac{\xi_\phi w_e}{8} (f_{keee} - 4f_{ke} + 6f_k - 4f_{kw} + f_{kww}), \quad (2.48)$$

$$\frac{\partial^4 f}{\partial \eta^4} = \frac{\eta_\theta w_e}{8} (f_{knkn} - 4f_{kn} + 6f_k - 4f_{ks} + f_{kss}), \quad (2.49)$$

where w_e is an adjustable parameter.

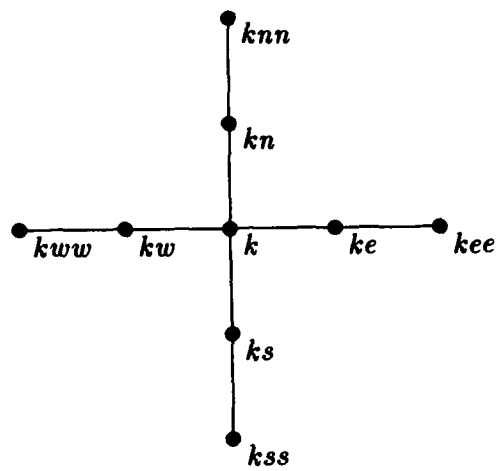


Figure 2.8 Stencil for fourth-order dissipation

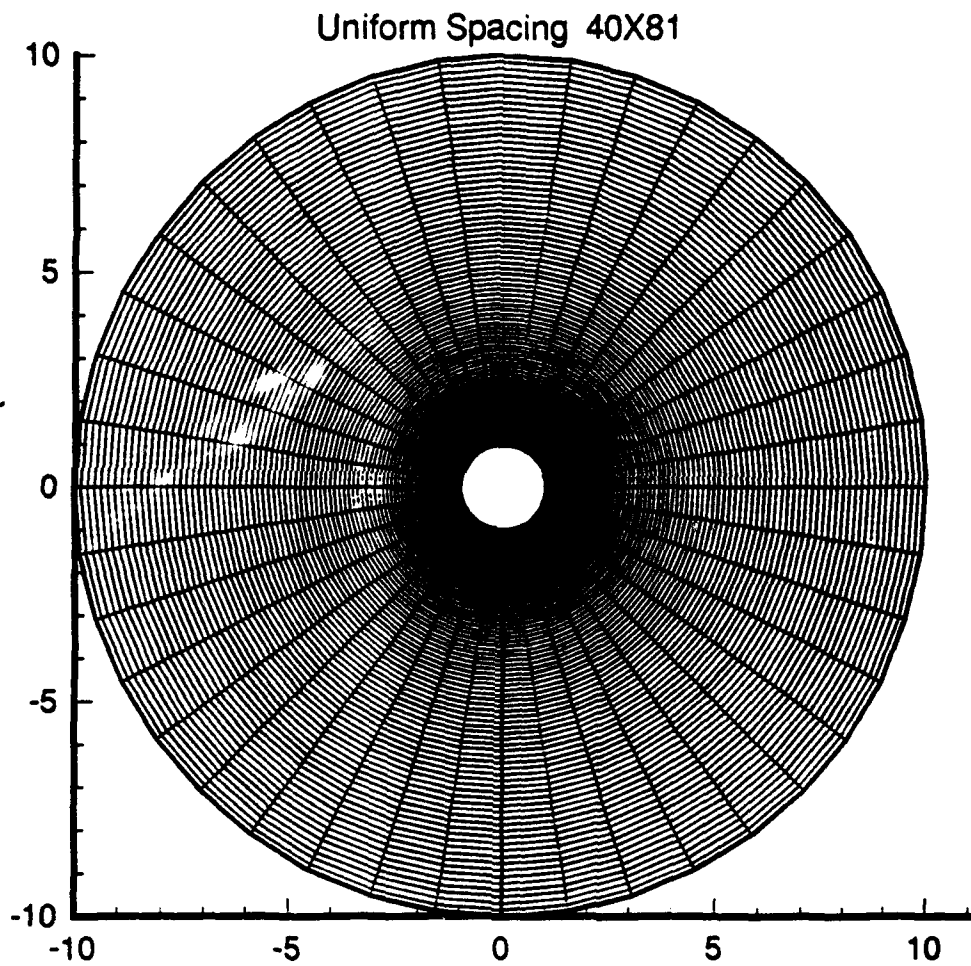


Figure 2.9 Uniform Grid

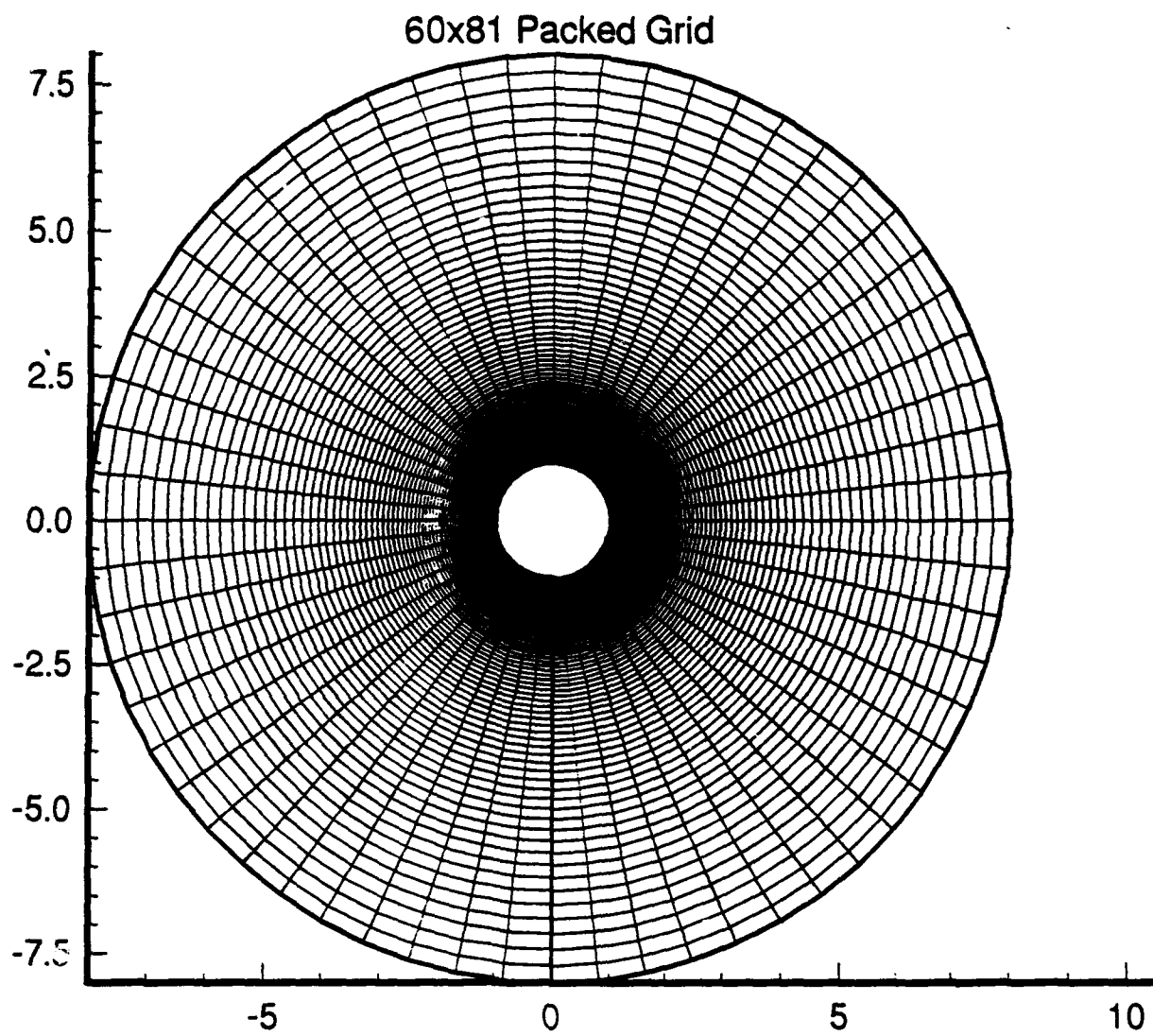


Figure 2.10 Packed Grid

III. Solution Algorithm

3.1 Newton's Method

Newton's method is an iterative scheme that solves the nonlinear system of equations of the form

$$\bar{F}(\bar{x}) = 0, \quad (3.1)$$

where \bar{x} is a vector of N unknowns, and \bar{F} is a set of N equations. The Newton iteration formula is

$$\bar{F}'_{\bar{x}}(\bar{x}^{\nu+1} - \bar{x}^{\nu}) = -\bar{F}(\bar{x}^{\nu}), \quad (3.2)$$

where $\bar{F}'_{\bar{x}}$ is the *Jacobian matrix*, whose elements are given by

$$\bar{F}'_{\bar{x}} = \begin{bmatrix} \frac{\partial F_1}{\partial x_1} & \frac{\partial F_1}{\partial x_2} & \dots & \frac{\partial F_1}{\partial x_n} \\ \frac{\partial F_2}{\partial x_1} & \frac{\partial F_2}{\partial x_2} & \dots & \frac{\partial F_2}{\partial x_n} \\ \vdots & \vdots & & \vdots \\ \frac{\partial F_n}{\partial x_1} & \frac{\partial F_n}{\partial x_2} & \dots & \frac{\partial F_n}{\partial x_n} \end{bmatrix}. \quad (3.3)$$

\bar{x}^{ν} represents a known solution state that is improved with the solution of (3.2), $\Delta\bar{x} = \bar{x}^{\nu+1} - \bar{x}^{\nu}$. Using central differences and a nine-point stencil to represent the derivatives in the governing equations, (3.2) results in a banded system that is solved using Gauss elimination. The solution of the system is $\Delta\bar{x} = \bar{x}^{\nu+1} - \bar{x}^{\nu}$. After each iteration, the approximate solution is updated by $\bar{x}^{\nu+1} = \Delta\bar{x} + \bar{x}^{\nu}$. Successive iterations are computed until the largest absolute $\Delta\bar{x}$ is less than some small value ϵ , or reaches machine zero. Newton's method is guaranteed to converge quadratically if the Jacobian matrix is non-singular and the initial guess is sufficiently close to the exact solution (18).

The analytical Jacobian elements are determined by differentiating each of the equations with respect to the unknown variables. An example of how these elements are derived is shown in Appendix B. For the discrete equations in this study, the Jacobian elements are

relatively complicated. There is always the chance that there are errors in the derivation and implementation of the elements. There are two methods of checking the accuracy of these elements. The first is if the scheme is quadratically convergent, then the Jacobian matrix is considered to be correct. The second method is to compare the analytical Jacobian elements with elements developed numerically. Using a method implemented by Morton (27), the elements of the two matrices are compared numerically, and when they are equal the analytical elements are considered correct. This numerical scheme consists of solving the function evaluation (right-hand side) for a given solution vector, \bar{x} , at each node, and then perturbing the solution vector by a small amount, $\bar{x} + \epsilon$, and then solving the function evaluation with the perturbed solution vector. Subtracting the two results for each unknown at each node in the nine-point stencil results in the numerical Jacobian elements. Since a finite perturbation is used ($\epsilon = 0.000001$), the accuracy of the numerical elements is taken to be one order less than the ϵ used. Use of this method allows for a systematic way of checking each of the Jacobian elements, since any differences in the two Jacobian matrices leads directly to the probable incorrect element. This allows the analytical Jacobian matrix to be verified with confidence in a short period of time. Without this type of comparison, there is always the possibility that incorrect development or implementation of the analytical Jacobian elements is the cause of any difficulties in obtaining a correct solution.

3.2 Continuation Method

It has been proven that if a solution \bar{x}^* is known and $\bar{F}_{\bar{x}}^*$ is nonsingular, then for some range of λ about λ^* there exists a unique solution path through (\bar{x}^*, λ^*) . The proof is outlined in (21). Pseudo-arclength continuation (PAC) is Keller's method of computing solutions along the solution path by using information at (\bar{x}^*, λ^*) to compute the next solution point.

Figure 3.1 is representative of a solution path found by plotting the norm of the solution vector versus the free parameter λ . The PAC process is to compute a tangent vector \bar{T} at a known solution \bar{x}^* , designated by P. Then at a distance d away, search along a line perpendicular to \bar{T} for the next solution point. This is done by first using arclength

to parameterize the solution path ($\bar{x} = \bar{x}(s)$, $\lambda = \lambda(s)$, and $\bar{F} = \bar{F}(s) = 0$). Then the tangent vector is computed by

$$\frac{d}{ds} \bar{F}(\bar{x}(s); \lambda(s)) = 0. \quad (3.4)$$

Using the chain rule, equation 3.5 becomes

$$\bar{F}_{\bar{x}}(s) \dot{\bar{x}}(s) + \bar{F}_{\lambda}(s) \dot{\lambda}(s) = 0, \quad (3.5)$$

where

$$\dot{\bar{x}}(s) \equiv \frac{d\bar{x}}{ds}(s), \quad (3.6)$$

and

$$\dot{\lambda}(s) \equiv \frac{d\lambda}{ds}(s). \quad (3.7)$$

The definition of arclength is

$$\|\dot{\bar{x}}\|^2 + \dot{\lambda}^2(s) = 1. \quad (3.8)$$

Equations 3.5 and 3.8 can then be solved as a system for the tangent vector:

$$\bar{T}(s) = \begin{pmatrix} \dot{\bar{x}}(s) \\ \dot{\lambda}^2(s) \end{pmatrix}, \quad (3.9)$$

providing the Jacobian matrix is not singular. Now define $\bar{\phi}$ such that

$$\bar{\phi} = \bar{F}_{\bar{x}}^{-1} \bar{F}_{\lambda}(s). \quad (3.10)$$

Then equations 3.5 and 3.8 give the following relationships

$$\dot{\lambda}(s) = \frac{\pm 1}{\sqrt{1 + \|\bar{\phi}\|^2}}, \quad (3.11)$$

and

$$\dot{\bar{x}}(s) = -\dot{\lambda}(s) \bar{\phi}. \quad (3.12)$$

The sign of equation 3.11 represents the direction of the tangent vector and is therefore indeterminate. At the startup of the continuation process this sign is set depending on which part of the solution path is to be computed.

From the solution P , the tangent vector T , and the distance d , the initial solution vector Q_0 can be computed:

$$\begin{pmatrix} \bar{x} \\ \lambda_{Q_0} \end{pmatrix} = \begin{pmatrix} \bar{x} \\ \lambda_P \end{pmatrix} + d \begin{pmatrix} \dot{\bar{x}} \\ \dot{\lambda}_P \end{pmatrix}. \quad (3.13)$$

The solution Q lies on a line perpendicular to T passing through Q_0 . This condition can be stated mathematically as

$$D \equiv \dot{\bar{x}}_P^T (\bar{x}_Q - \bar{x}_P) + (\lambda_Q - \lambda_P) \dot{\lambda}_P = d \quad (3.14)$$

and can be added to the system of nonlinear equations 3.1. This new system is then solved by Newton's method with Q_0 as the initial guess. Q_0 becomes a better and better first approximation as d gets smaller. The solution \bar{x}_Q is obtained when $F = 0$ and $D = d$. Another solution can be computed by repeating the process.

The entire section on the continuation method was taken directly from Morton (26).

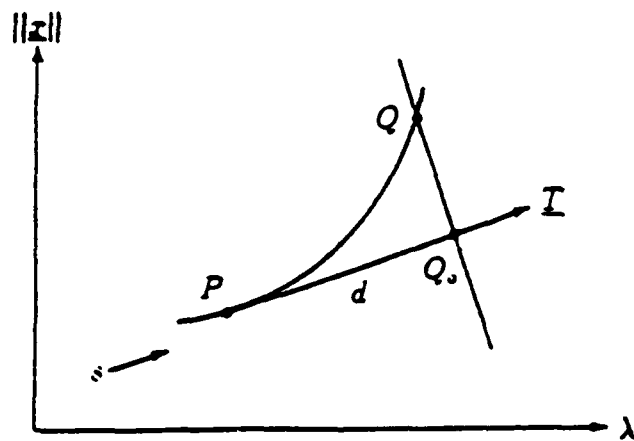


Figure 3.1 Illustration of continuation procedure, Beran (4)

IV. Navier-Stokes Solutions

Initially, the boundary conditions in Table 4.1 were used to solve the subsonic flow over a slender cone at zero angle of attack. These boundary conditions are the same as those used by Degani and Schiff (10) in their three-dimensional analysis. However, when these boundary conditions are used, oscillations (odd-even decoupling) developed in the computed flow variables ρ , u , v , w , and e . A significant amount of effort was spent trying to find an error in the code that would account for an error of this type. The derivation of the governing equations was checked by two independent methods, outlined in Appendix A. The derivation of the analytical Jacobian elements and their implementation in the code was checked using the numerical procedure outlined in Chapter III. The placement of the Jacobian elements into the matrix was checked extensively, especially in the grid separation region. Finally, a comparison was made with a 1-D inviscid code at $\alpha = 0$, using the boundary conditions in Table 4.2. These boundary conditions represent slip flow and impermeability at the wall boundary. The two methods gave the same numerical result, both having oscillations in the computed solution. The addition of fourth-order numerical dissipation, outlined in Chapter 2.9, did not reduce the oscillations. Next, the boundary conditions in Table 4.2 were used for a supersonic inviscid model at $\alpha = 0$, and the solution matched that of exact methods, both in shock angle and velocity components. The results of this analysis is presented in Section 4.1. This analysis helped to verify the correctness of some of the computer code, especially the implementation of the Jacobian elements in the separation region. At this stage, the freestream boundary conditions were suspected as the cause of the oscillatory behavior in the solution.

Several attempts were made to develop freestream boundary conditions for which the solution would be free of oscillations. Several variations were attempted, and the boundary conditions outlined in Table 4.3 and Table 4.4 were found to give good results. The key to the problem is how the continuity equation is implemented at the discrete node points. Initially, the continuity equation was used as a freestream boundary condition, as well as one of the governing equations for the interior nodes. This method still resulted in oscillatory behavior. Then, the continuity equation was evaluated at the midpoint between the node in question, k , and the next node closer to the wall, ks (see Figure 2.6), for both

boundary and interior continuity equations. This allows the use of second-order-accurate difference approximations for the freestream boundary derivatives while only using two nodes instead of three. Good results were obtained depending on the number of grid points along each radial line relative to the difference between the cone halfangle, θ_c , and the angle of the freestream boundary, θ_{max} . If enough points were placed along each radial line, then the solution was free of oscillations. This appeared to be only a partial fix to the problem, as this method was very dependent on how many nodes were placed along each radial line. The method that gave the best results was to evaluate the continuity equation at node k for the interior node points, and at the midpoint of node k and node ks for the freestream boundary condition. A more detailed explanation of this method is outlined in Chapter 2.7.

Wall	Freestream
$\frac{\partial \rho}{\partial n} = 0$	$\rho = 1$
$u = 0$	$u = u_{fs}$
$v = 0$	$v = v_{fs}$
$w = 0$	$w = w_{fs}$
$\frac{\partial e}{\partial n} = 0$	$e = e_{fs}$

Table 4.1 Initial boundary conditions for viscous subsonic flow

Wall	Freestream
$\frac{\partial \rho}{\partial n} = 0$	$\rho = 1$
$\frac{\partial u}{\partial n} = 0$	$u = u_{fs}$
$v = 0$	$v = v_{fs}$
$w = 0$	$w = w_{fs}$
$\frac{\partial e}{\partial n} = 0$	$e = e_{fs}$

Table 4.2 Initial boundary conditions for inviscid subsonic flow

4.1 Supersonic Results

These results were obtained as part of a validation procedure for the analysis. This investigation provided assurance that the Jacobian elements were being placed correctly in the Jacobian matrix, and the basic logic of the computer code was correct. Figure 4.1,

from (2), shows the pertinent parameters for this problem. All of the results in this section were obtained for $\alpha = 0$.

For supersonic, inviscid, axisymmetric flow, the governing equations (2.15 - 2.19) reduce to:

$$2\rho u \sin\theta + (\rho v \sin\theta)_\theta = 0, \quad (4.1)$$

$$\rho [vu_\theta - v^2] = 0, \quad (4.2)$$

$$\rho \left[\left(\frac{v^2}{2} \right)_\theta + uv \right] + (\gamma - 1)(\rho e)_\theta = 0, \quad (4.3)$$

$$w = 0, \quad (4.4)$$

$$\rho[ve_\theta] + (\gamma - 1)e\rho[2u + v \cot\theta + v_\theta] = 0. \quad (4.5)$$

Compared to the governing equations in Chapter 2.3, some of the terms in the equations are cast in a more conservative form to better resolve the shock position. Several runs were made at varying Mach numbers and the resulting shock positions are compared to published data (28) in Table 4.1. These runs were made with six radial lines around the cone and either 201 or 401 node points equally spaced along each radial line. A cone angle, θ_c , of five degrees was selected; the outer radius of the domain was specified to be 50 degrees ($\theta_{max} = 50$). For all cases examined, the shock angles agree very well, especially when 401 nodes are used. The shock angle is determined by examining the non-dimensional density between the cone and the freestream boundary. As shown in Figure 4.2, the density varies from a value greater than one near the cone, to a value that is nearly one at the shock. The shock angle is determined to be located at the first node (starting from the cone) where the density becomes one (equal to the freestream non-dimensional density). For the example detailed in Figure 4.2, the Mach number is 1.321, and the estimated shock angle is 49.375 deg. With 401 nodes used in the radial direction, and a difference in θ_c and θ_{max} of 50 degrees, the angular change between nodes is 0.125 deg. Therefore, the next computational node closer to the cone is located at 49.25 deg. From (22), the exact shock angle is 49.262 deg, which lies in between the two computational nodes outlined above. If needed, further refinement of the computational domain will give better resolution.

Figures 4.3 and 4.4 show the computed values of the non-dimensional velocity components u , v as compared to the exact values, computed using the Taylor-Maccoll equations and tabulated in (22). These results agree extremely well over the entire region between the shock and the wall. These results are for a Mach number of 1.321, chosen to match one of the tables in (22).

4.2 Subsonic Results

Several point solutions were attempted in the development of the solution algorithm. The effect of the bandwidth on the size of the Jacobian matrix has been outlined in Chapter II. As the bandwidth increased, the computational speed decreased. In addition, increasing the bandwidth also increased the memory requirements. These two constraints imposed a limit on the size of the grid that could be used in the analysis. This in turn limits the parameters used in a point solution. Point solutions at varying angles of attack were computed for the flow parameters outlined in Table 4.6. The number of nodes around the cone was varied between 30, 50, and 81, and the number of nodes between the wall and the body kept at 81. The results, presented as contour plots of non-dimensional pressure, are shown in Figures (4.5 - 4.14). These plots are correct qualitatively, although no comparison with published data could be accomplished due to the low Reynolds number being used at this time. Figure 4.15 shows the coefficient of pressure at the cone surface for the three different grids. There is virtually no change in the pressure coefficient as the grid is changed, indicating that at least for this case the boundary layer is being resolved correctly and the solution very close to the body is independent of the grid. The values of the pressure coefficient as a function of ϕ are consistent with published data, though no direct comparison could be made at this run condition.

At first, the computer used for this project was only capable of handling a 30x81 grid. For this grid, attempts were made to vary the amount of artificial dissipation added to the model. It was expected that the added dissipation would help smooth the pressure contours away from the body, where the grid coarseness is evident. However, as more dissipation was added, the convergence behavior became worse. This indicates an error in the implementation of the artificial dissipation, which has not been discovered at this time.

Solutions at higher Reynolds numbers ($Re = 5000$) were attempted, but the convergence behavior was poor. As the Reynolds number is increased, the boundary layer becomes thinner. This requires greater resolution near the wall, which means there will be less resolution away from the wall, assuming the same number of nodes are being used. Because of the constraint on the number of nodes due to the memory requirements, increasing the Reynolds number makes it harder and harder for the solution to converge.

At this point a different computer platform became available. This new platform had a significant increase in the amount of available memory, as well as computational speed. The code was implemented on this machine, and grids of 50×81 and 60×81 were now possible. Several point solutions were calculated, using the parameters outlined in Table 4.6. As can be seen from the pressure contour plots, the additional nodes around the body helped to smooth the contours near the body, but there is still evidence of spurious results away from the body. At these grids, a point solution required several hours to complete. Therefore, the main effort of the project shifted to finding ways to speed up the code. With the implementation of a block structure gauss elimination routine, the speed of the code was eventually increased by a factor of four or five. Efforts were also made in implementing methods that would decrease the memory requirements of the program, allowing for larger grids being used. These modifications were only recently made, and the memory savings they provide could not be taken advantage of for this study.

Addition of the continuation method to the algorithm was accomplished. With this method, a point solution is computed at zero angle of attack to determine the sign of the determinate of the Jacobian matrix. Then continuation occurs in an attempt to locate the bifurcation point, if one exists. This point is located when the sign of the determinate changes. Once the bifurcation point is located, the solution method is perturbed by a small value so the nontrivial solution path can be explored (see Figure 1.2a). Only manual continuation was attempted in this study. No evidence of a bifurcation point was discovered, but without a grid sensitivity study, there is no way to determine if this or any other result is accurate. Also, the Reynolds number used in this study ($Re = 500$), may be too small for this type of analysis.

It should be noted that while all of the original goals of this project were not completed, a significant amount of work was accomplished. All of the tools required for the completion of the analysis have been developed. The computer program has been debugged and validated. The continuation method was implemented, and several efforts were made to increase the speed of the code, as well as decrease the memory requirements.

Wall	Freestream Boundary
$\frac{\partial \rho}{\partial n} = 0$	continuity
$\frac{\partial u}{\partial n} = 0$	$u^2 + v^2 + w^2 = 1$
$v = 0$	$\rho = 1$
$\frac{\partial w}{\partial n} = 0$	$w = w_{fs}$
$\frac{\partial e}{\partial n} = 0$	$e = e_{fs}$

Table 4.3 Boundary conditions for subsonic, inviscid flow

Wall	Freestream Boundary
$\frac{\partial \rho}{\partial n} = 0$	continuity
$u = 0$	$u^2 + v^2 + w^2 = 1$
$v = 0$	$\rho = 1$
$w = 0$	$w = w_{fs}$
$\frac{\partial e}{\partial n} = 0$	$e = e_{fs}$

Table 4.4 Boundary conditions for subsonic, viscous flow

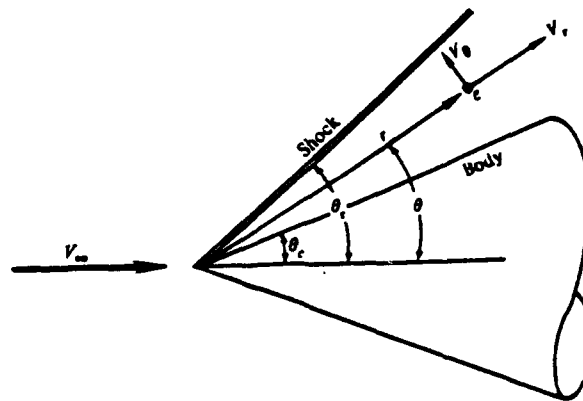


Figure 4.1 Supersonic Flow over Cone at $\alpha = 0$

6x401				6x201
θ_c	M	θ_{cal}	θ_{table}	θ_{cal}
10	2.0	30.3	31	
5	1.2	56.8	56.6	57.15
5	1.4	45.95	45.6	45.95
5	1.6	38.95	38.8	39.3
5	1.8	34.05	34.9	34.4
5	2.0	30.38	30.2	30.55
5	2.2	27.4	27.2	27.75
5	2.4	25.13	24.9	25.3
5	2.6	23.03	24.9	23.2

Table 4.5 Shock angle results

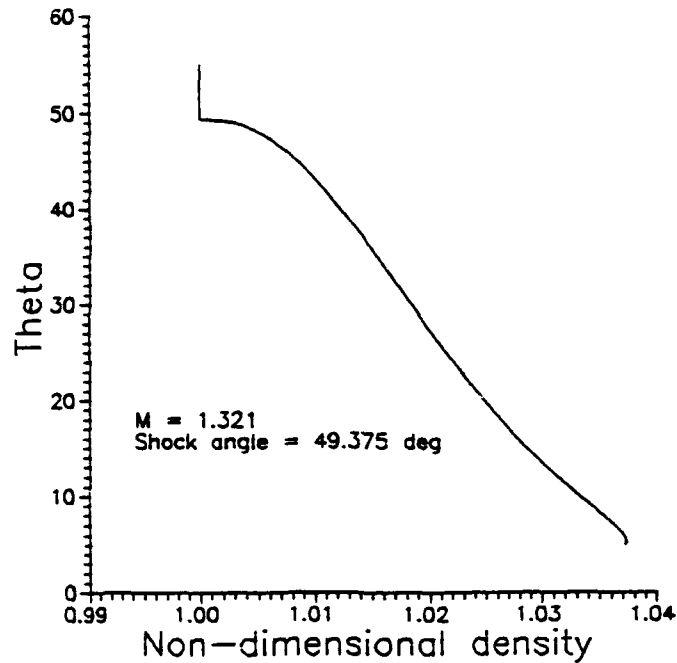


Figure 4.2 Non-dimensional density

$M = 0.3$
$\theta_c = 5 \text{ deg}$
$\theta_{max} = 50 \text{ deg}$
$Re = 500$
$Pr = 0.71$
$d_{min} = 0.001$
$T_{\infty} = 300 \text{ K}$
$P_{\infty} = 7.936508$

Table 4.6 Run Conditions for Point Solutions

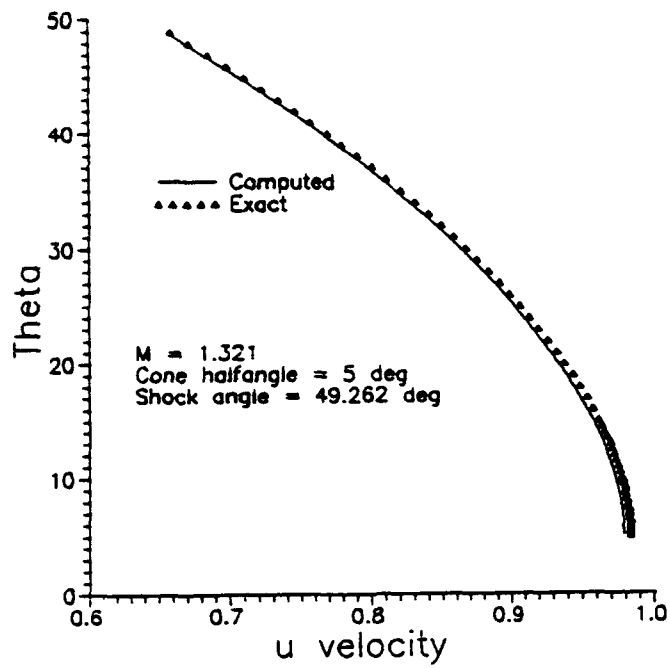


Figure 4.3 Non-dimensional u velocity component

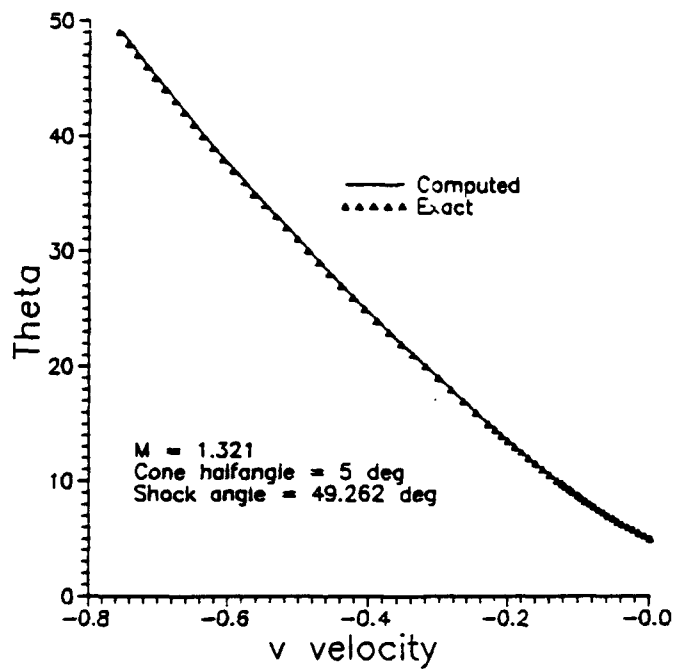


Figure 4.4 Non-dimensional v velocity component

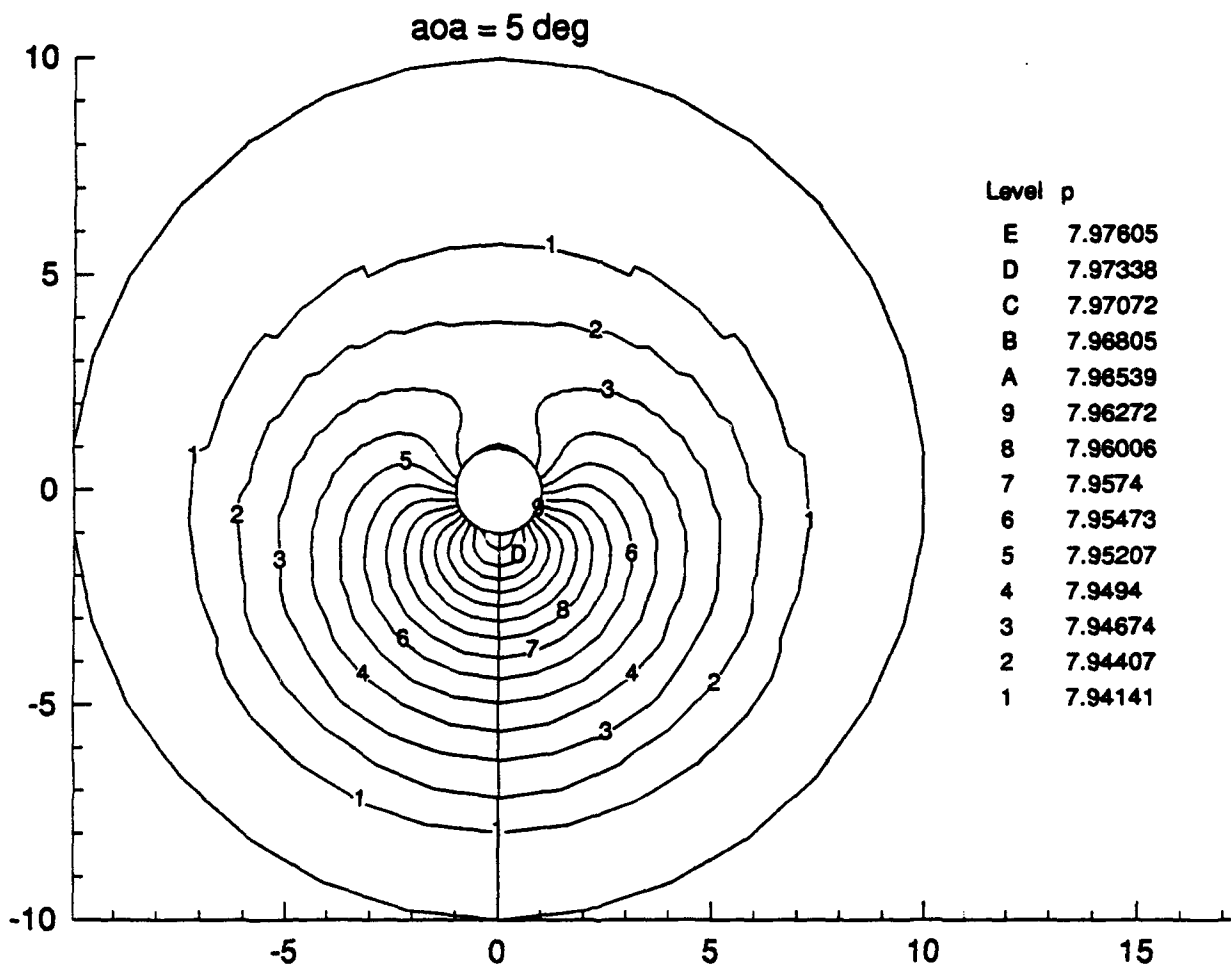


Figure 4.5 30x81, $Re = 500$, $M = .3$, $\alpha = 5$ deg

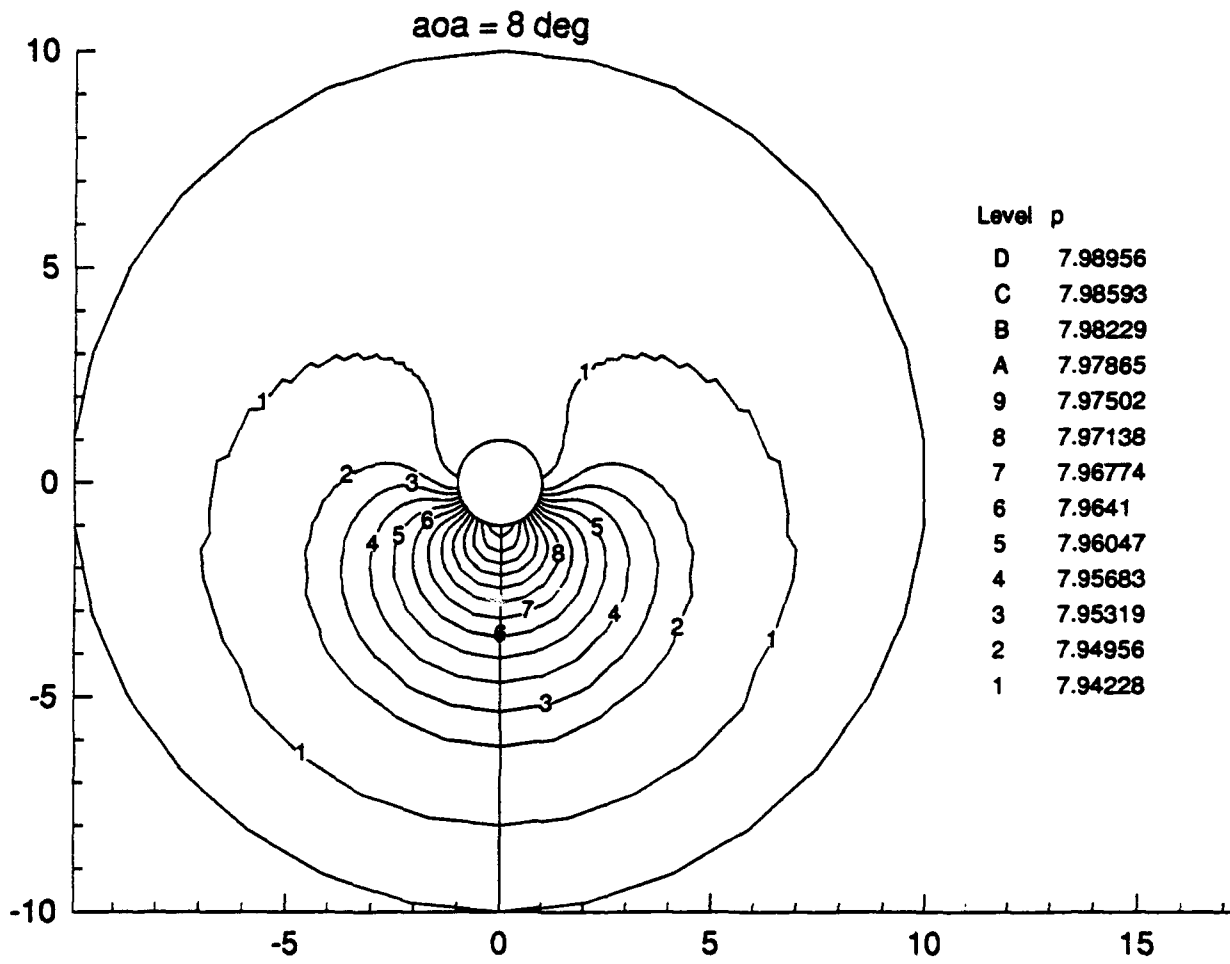


Figure 4.6 30x81, $Re = 500$, $M = .3$, $\alpha = 8$ deg

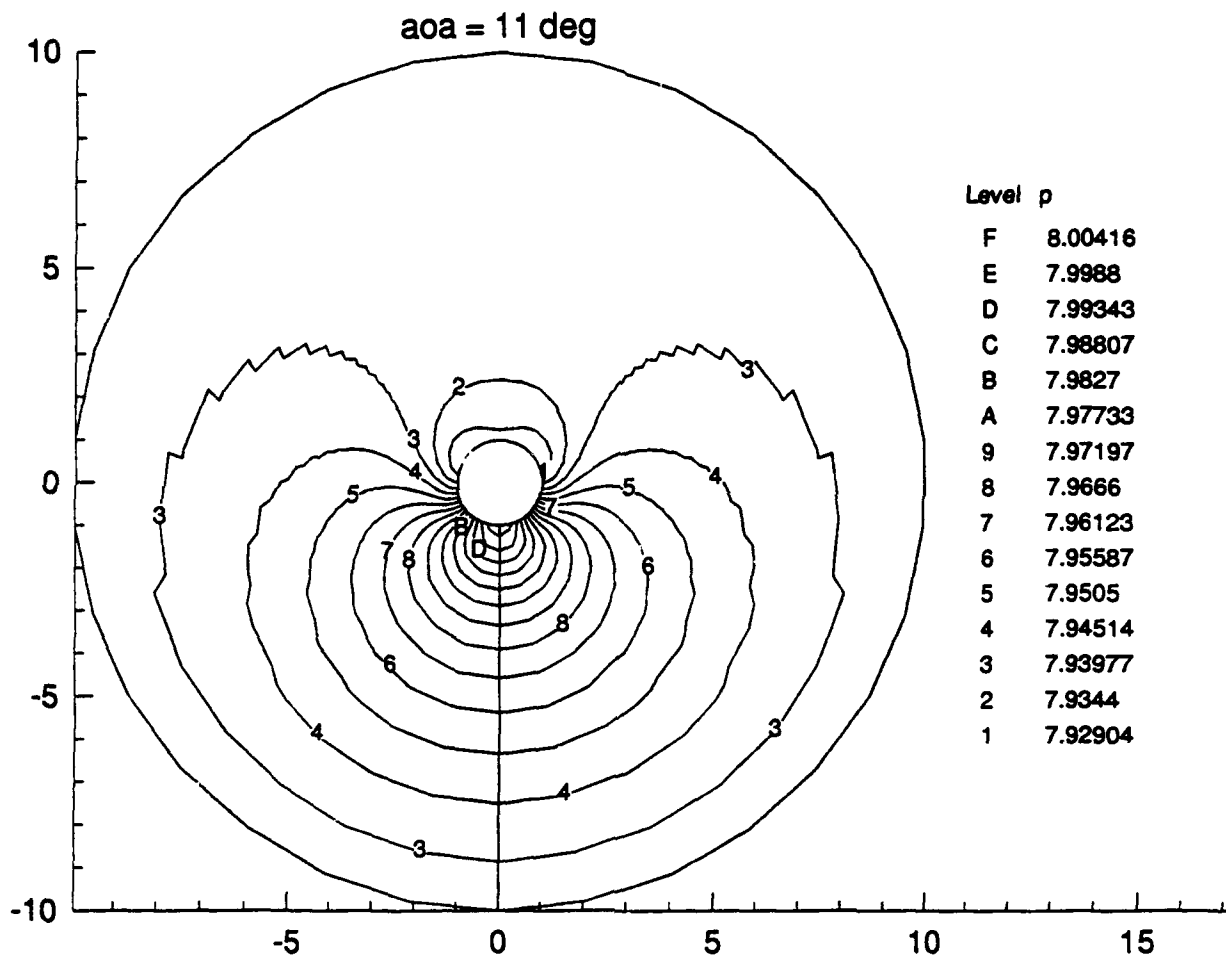


Figure 4.7 30x81, $Re = 500$, $M = .3$, $\alpha = 11$ deg

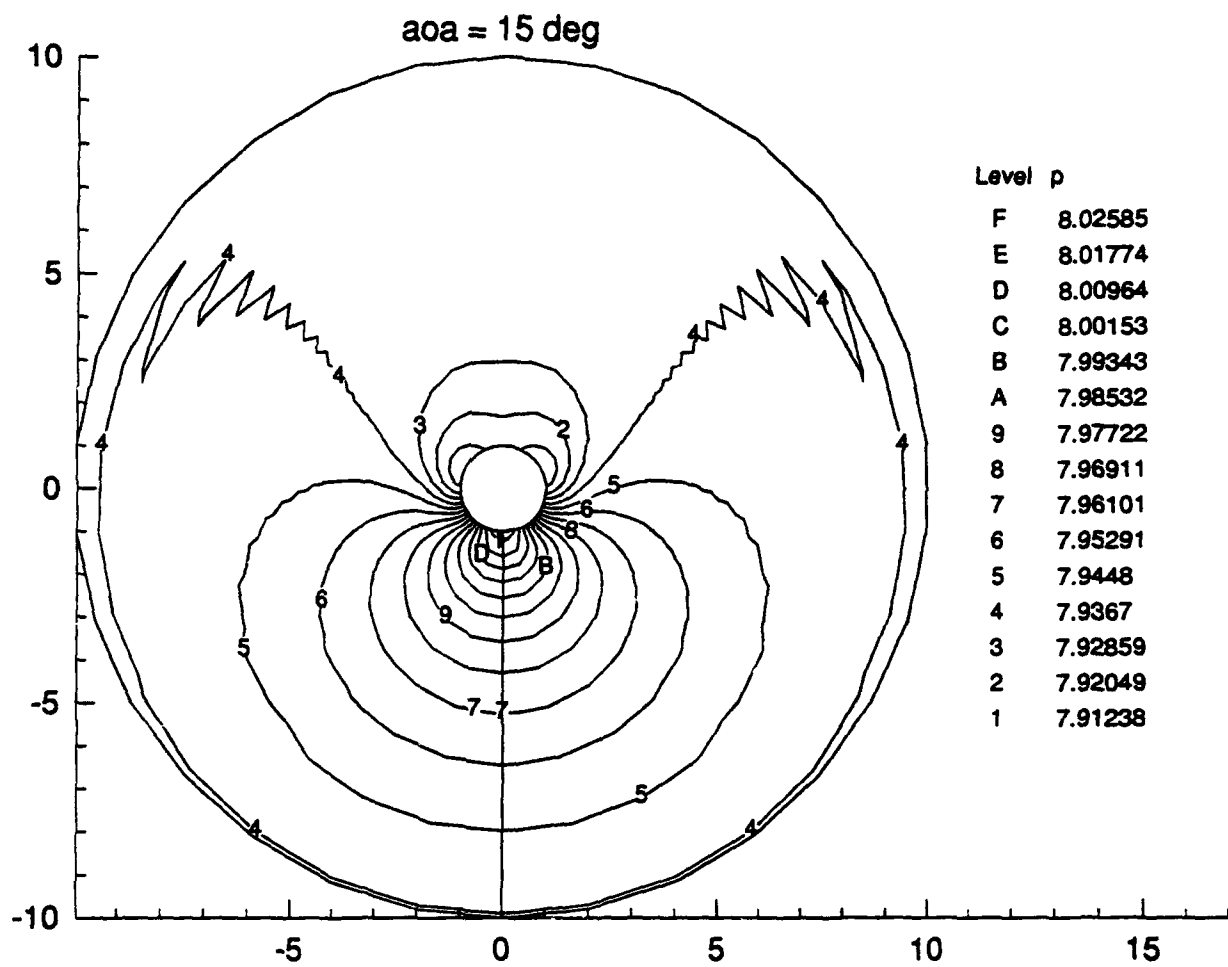


Figure 4.8 30x81, $Re = 500$, $M = .3$, $\alpha = 15$ deg

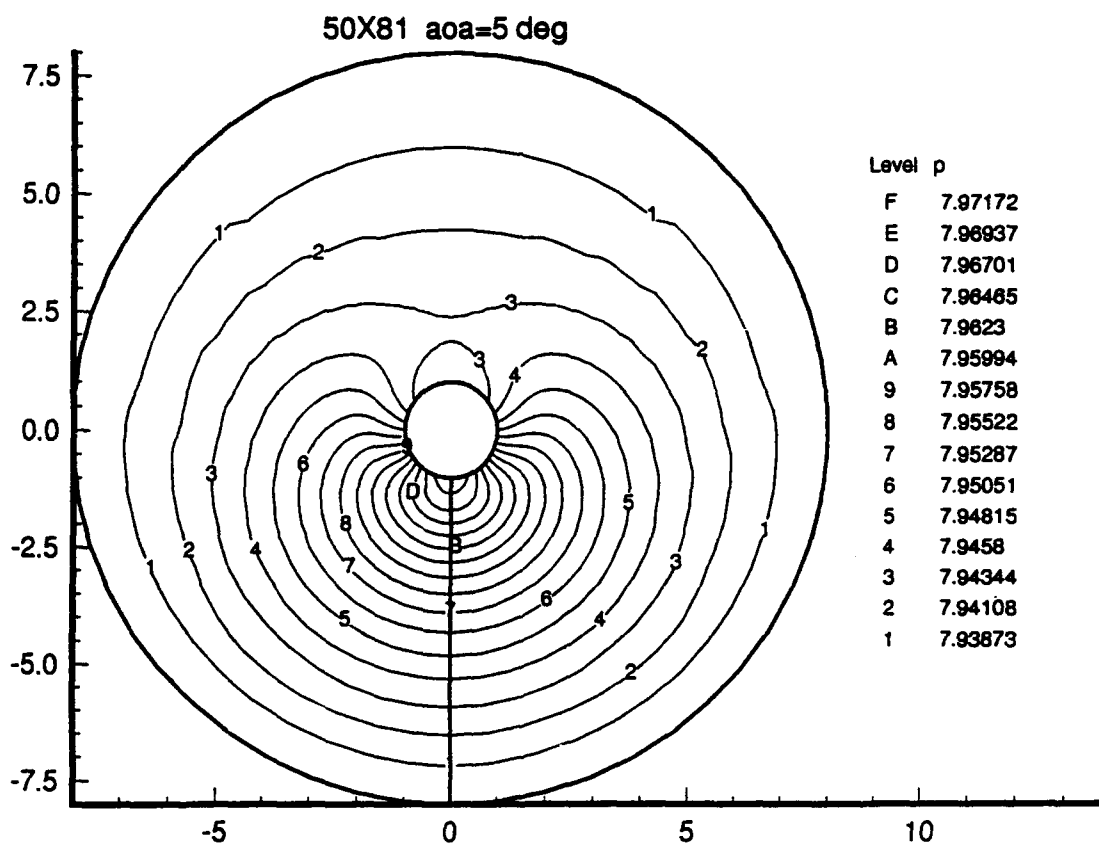


Figure 4.9 50x81, $Re = 500$, $M = .3$, $\alpha = 5$ deg

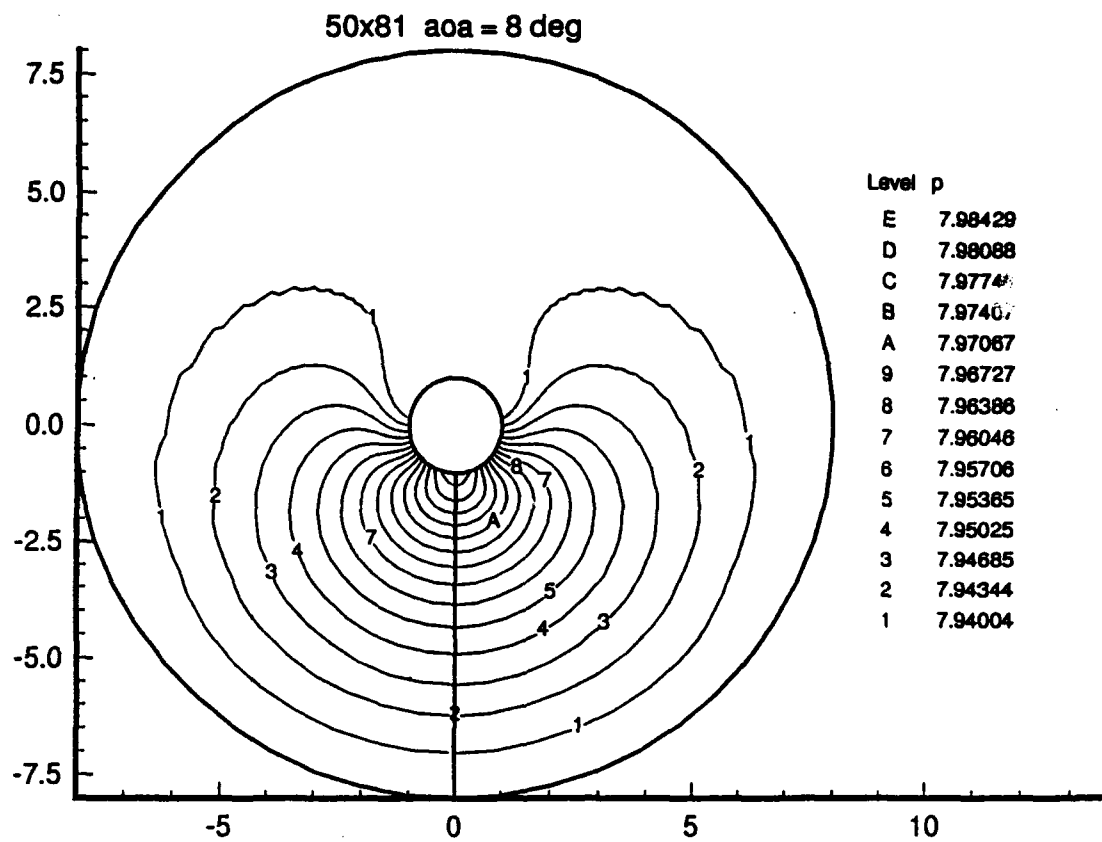


Figure 4.10 50x81, $Re = 500$, $M = .3$, $\alpha = 8$ deg

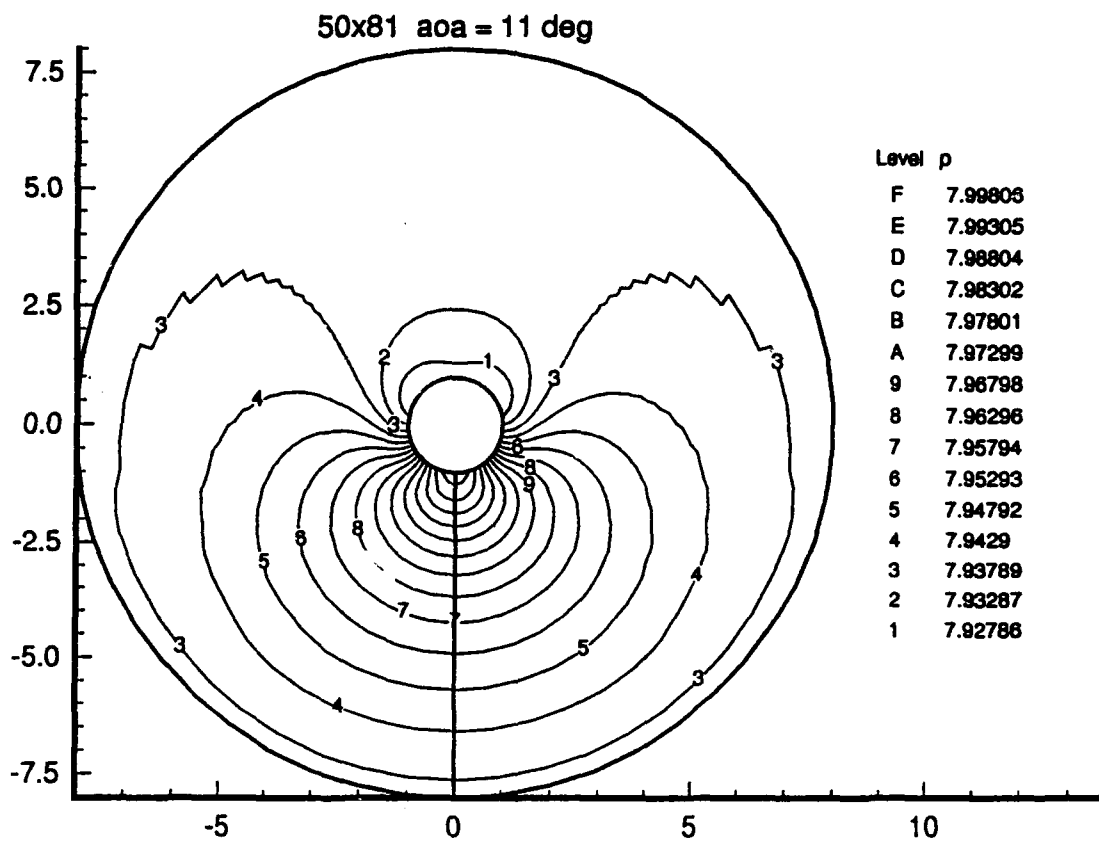


Figure 4.11 50x81, $Re = 500$, $M = .3$, $\alpha = 11$ deg

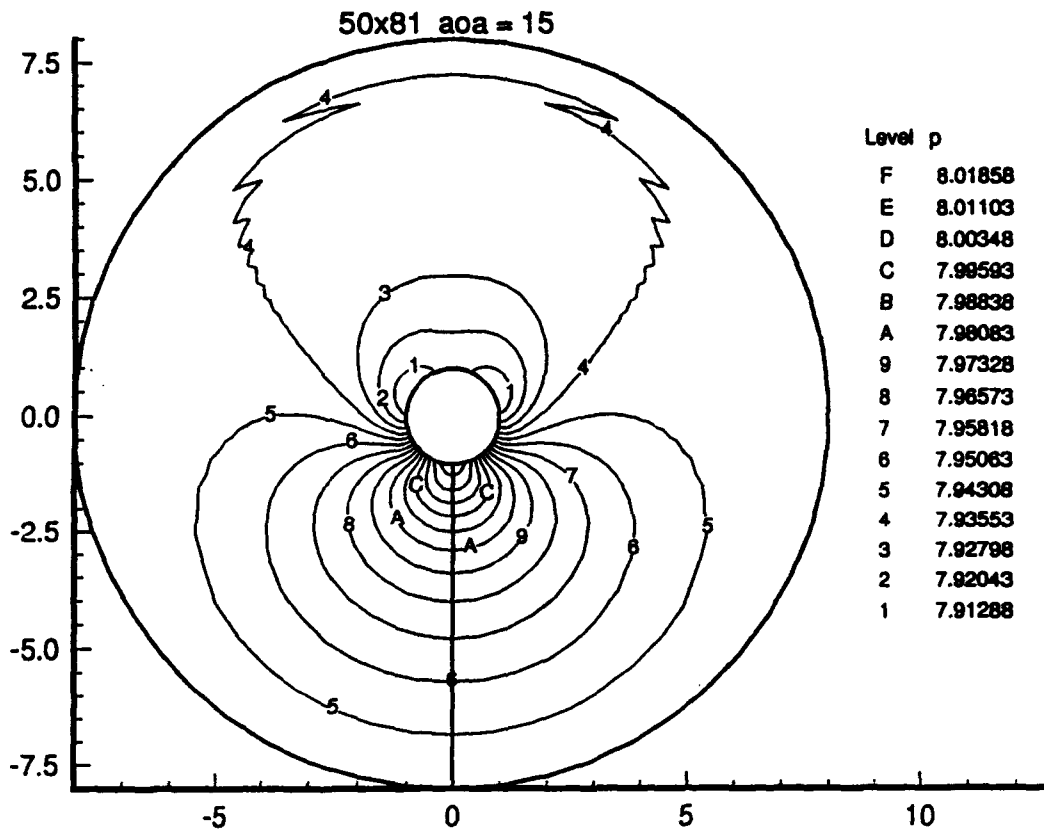


Figure 4.12 50x81, $Re = 500$, $M = .3$, $\alpha = 15$ deg

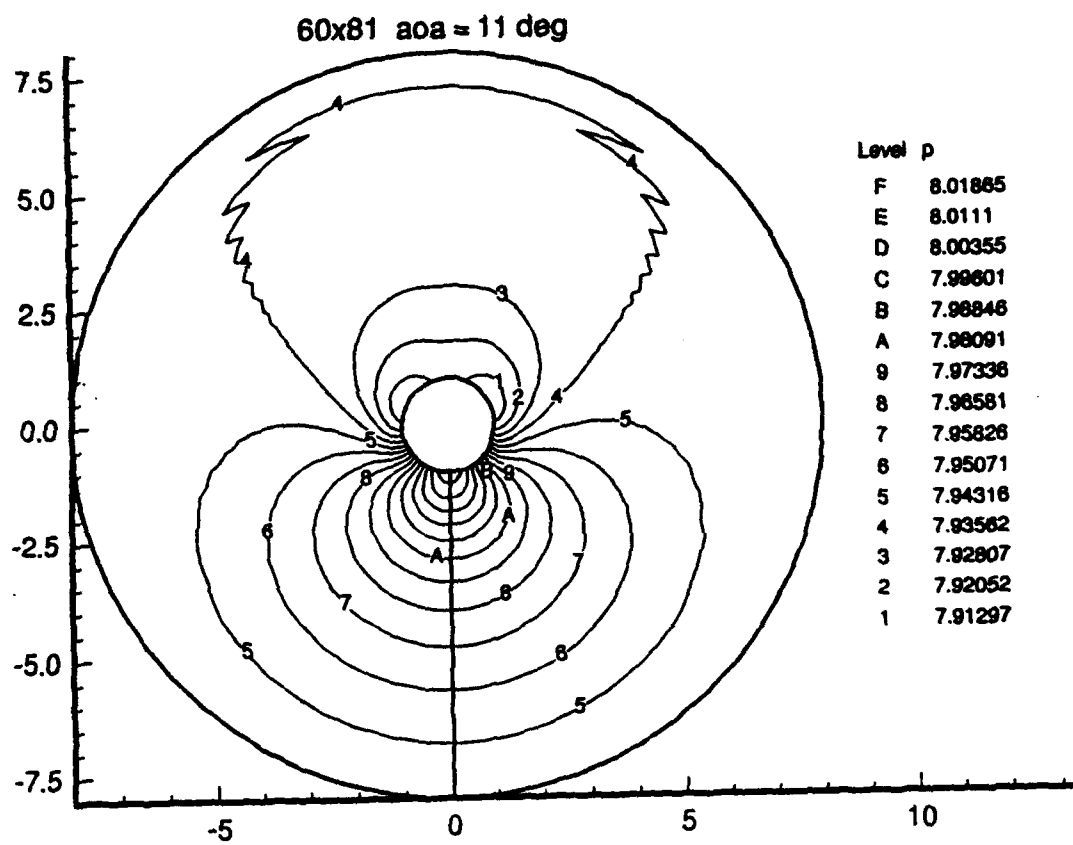


Figure 4.13 60x81. $Re = 500, M = .3, \alpha = 11$ deg

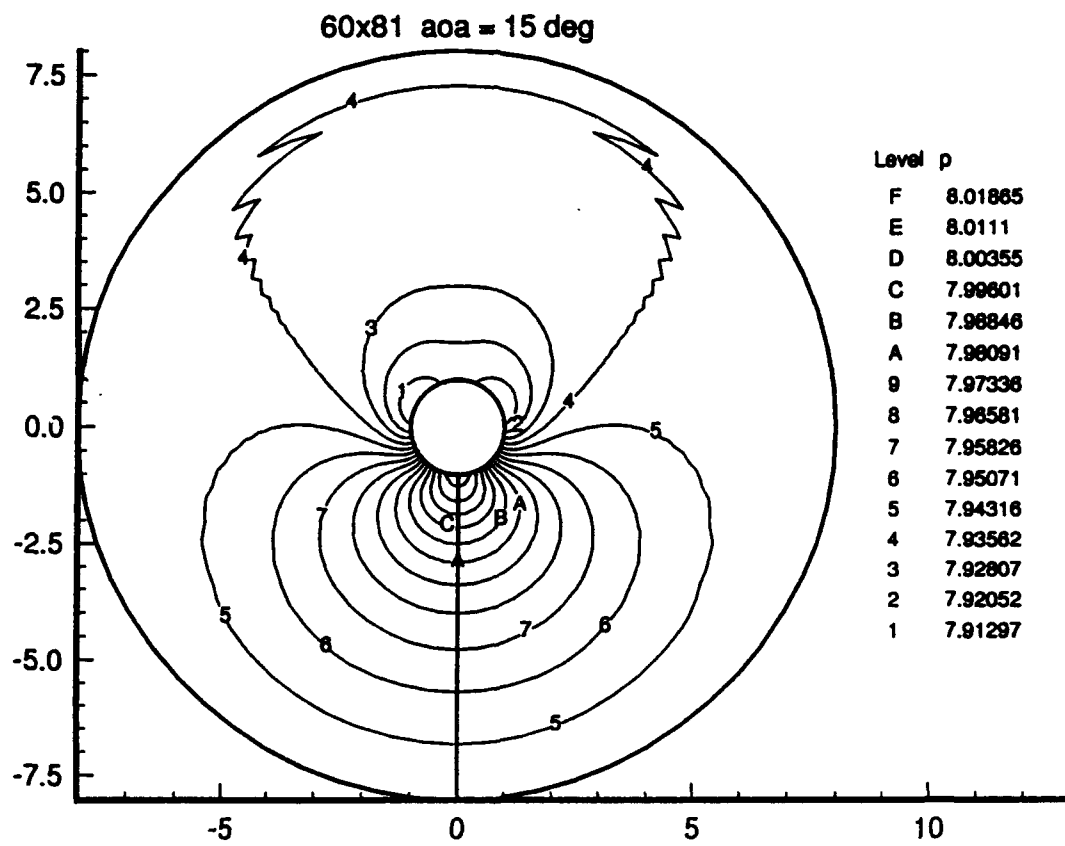


Figure 4.14 60x81. $Re = 500$, $M = .3$, $\alpha = 15$ deg

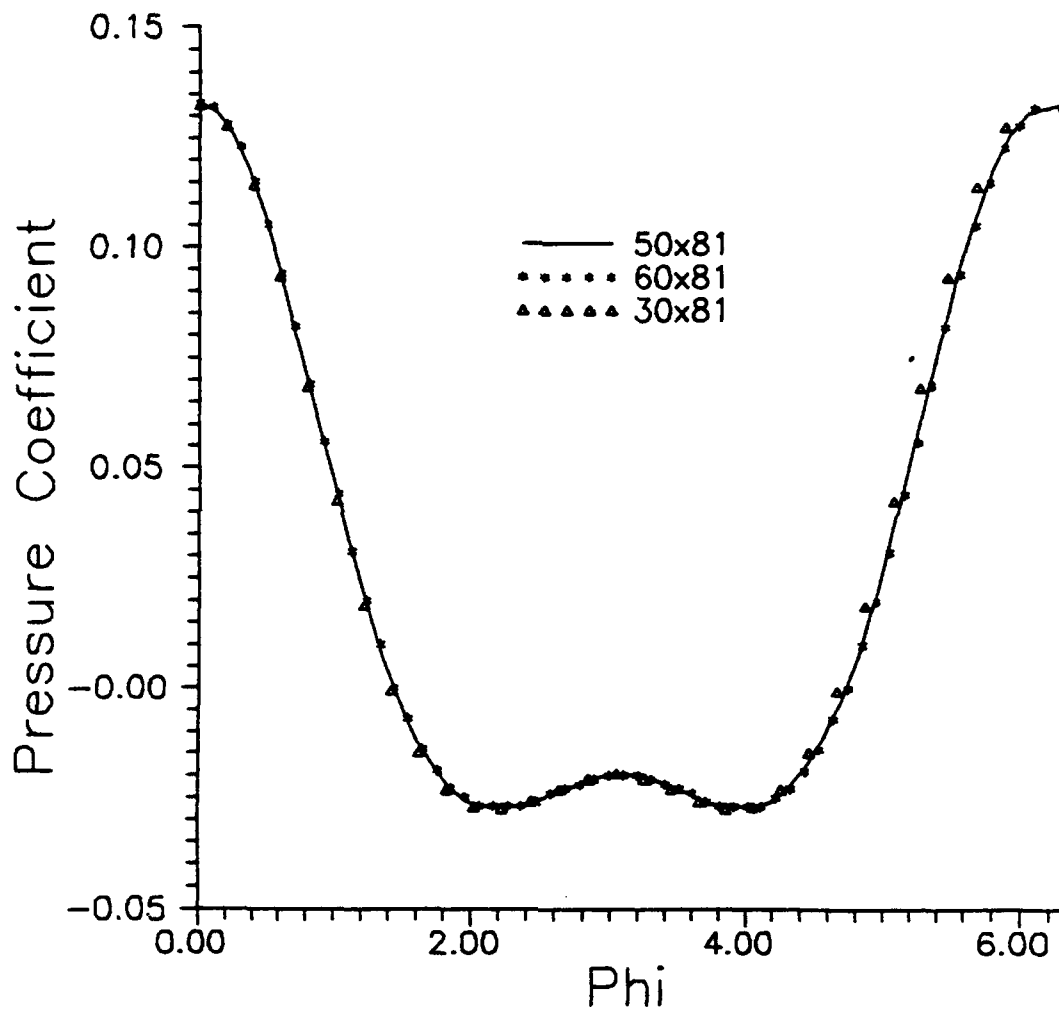


Figure 4.15 Pressure Coefficients

V. *Conclusions and Recommendations*

The compressible, laminar, viscous Navier-Stokes equations were solved for subsonic flow over a slender circular cone at angle of attack. A supersonic, inviscid study was performed at zero angle of attack as a validation of the solution implementation. Excellent results were obtained for the supersonic cases, where the shock angle and velocity components were calculated and compared to tabulated results.

Several point solutions were calculated for varying angles of attack, and for different grid sizes. A continuation method was implemented, which is used to locate the bifurcation point, if one exists. For this investigation, only manual continuation was used.

The most obvious problem that needs to be analyzed is the bandwidth influence on computational speed and memory requirements. With the row-by-row numbering scheme, the driving requirement is the use of second-order-accurate approximations for the boundary derivatives at the wall. First-order-accurate approximations could be used, but the loss of accuracy makes this undesirable. An alternative solution is to modify the computer code so that the analytical Jacobian elements are stored in single precision. When any computations are made with these elements, double precision would be used. This effectively cuts the memory requirements of the computer code in half. There is some loss of accuracy and convergence rate, but these disadvantages should be tolerable.

Recent analysis has dealt with speeding up the code by modifying the structure of the matrix so that the system of equations could be solved using a blocked method. This has been implemented and the result is a significant speed up of the code. Unfortunately, this does nothing for the memory issue.

Much more effort is required to complete all the analysis necessary to determine if asymmetric vortices are a real solution of the Navier-Stokes equations. An extensive study of the grid, and its effect on the solution needs to be performed. Areas of interest include, but are not limited to, grid refinement in both the ϕ and θ directions, choosing an amount of artificial dissipation that allows for a smooth solution without destroying the accuracy of the results near the body, examining the effect of the boundary conditions on the results, and examining the boundary layer resolution by investigating solutions

at different Reynolds numbers. Analysis of this type will help to characterize the length scales in the problem, and determine whether a particular grid will resolve all of these length scales. Once a set of parameters is determined that will result in a grid independent solution, continuation can be used, either manual or implemented in the program, to vary the angle of attack in an attempt to locate a bifurcation point. If this step is reached, the solution method implemented in this computer model can be used to describe all branches in the solution space. whether stable or unstable.

Bibliography

1. Anderson, D.A., Tannehill, J.C., and Pletcher, R.H. 1984 *Computational Fluid Mechanics and Heat Transfer*. Hemisphere, New York.
2. Anderson, J.D. 1982 *Modern Compressible Flow*. McGraw-Hill, New York.
3. Batina, J.T. 1989 Vortex-Dominated Conical-Flow Computations Using Unstructured Adaptively-Refined Meshes. *AIAA Paper* 89-1816.
4. Beran, P.S. 1989, An investigation of the Bursting of Trailing Vortices Using Numerical Simulation. Ph.D. Thesis, California Institute of Technology.
5. Burden, R.L. and Faires, D. 1993 *Numerical Analysis*. PWS-KENT, Boston.
6. Buter, T.A. Class handout, AERO 752, Computational Aerodynamics. School of Engineering, Air Force Institute of Technology, Wright-Patterson AFB OH, March 1993.
7. Degani, D. 1990 Numerical Investigation of the Origin of Vortex Asymmetry. *AIAA Paper* 90-0593.
8. Degani, D. 1992 Instabilities of Flows over Bodies at Large Incidence. *AIAA Journal*, **30** (1), 94.
9. Degani, D., and Levy, Y. 1992 Asymmetric Turbulent Vortical Flows over Slender Bodies. *AIAA Journal*, **30** (9), 2267.
10. Degani, D. and Schiff, L.B. 1989 Numerical Simulation of the Effect of Spatial Disturbances on Vortex Asymmetry. *AIAA Paper* 89-340.
11. Dyer, D.E., Fiddes, S.P., and Smith, J.H.B. 1982 Asymmetric Separation from Cones at Incidence - A Simple Inviscid Model. *Aeronautical Journal*, **33**, 293.
12. Ericsson, L.E. 1993 Thoughts on Conical Flow Asymmetry. *AIAA Journal*, **31** (9), 1563.
13. Ericsson, L.E., and Reding, J.P. 1980 Vortex-Induced Asymmetric Loads in 2-D and 3-D Flows. *AIAA Paper* 80-0181.
14. Fiddes, S.P. "Separated Flow About Cones at Incidence - Theory and Experiment," *Studies of Vortex Dominated Flows*. edited by M.Y. Hussaini and M.D. Salas, Springer-Verlag, New York, 1985.
15. Fiddes, S.P., and Smith, J.H.B. 1982 Calculation of Asymmetric Separated Flow Past Circular Cones at Large Angles of Incidence. *AGARD Report* CP-336.
16. Hoffmann, K.A. 1989 *Computational Fluid Dynamics for Engineers*. Engineering Education System, Austin.
17. Hughes, W.F. and Gaylord, E.W. 1964 *Basic Equations of Engineering Science*. McGraw-Hill, Inc., New York.
18. Isaacson, E., and Keller, H.B. 1966 *Analysis of Numerical Methods*. John Wiley & Sons, New York.
19. Kandil, O.A., Wong, T., and Liu, C.H. 1991 Prediction of Steady and Unsteady Flows Around Circular Cones. *AIAA Journal*, **29** (12), 2169.

20. Keener, E.R., and Chapman, G.T. 1977 Similarity in Vortex Asymmetries over Slender Bodies and Wings. *AIAA Journal*, **15** (9), 1370.
21. Keller, H.B. 1982 Continuation Methods in Computational Fluid Dynamics. *Numerical and Physical Aspects of Aerodynamic Flows*, (ed. T. Cebici). Springer-Verlag, New York.
22. Kopal, Z. Tables of Supersonic Flow around Cones. MIT TR No. 1, 1947.
23. Lowson, M.V., and Ponton, A.J.C. 1992 Symmetry Breaking in Vortex Flows on Conical Bodies. *AIAA Journal*, **30** (6), 1576.
24. Marconi, F. "Asymmetric Separated Flows about Sharp Cones in a Supersonic Stream," *11th International Conference on Numerical Methods in Fluid Dynamics*, edited by D.L. Dwoyer, M.Y. Hussaini, and R.G. Voigt, Springer-Verlag, Berlin, 1988.
25. Modi, V.J., Cheng, C.W., and Mak, A. 1992 Reduction of the Side Force on Pointed Forebodies Through Add-On Tip Devices. *AIAA Journal*, **30** (10), 2462.
26. Morton, S.A. 1989 Numerical Simulation of Compressible Vortices. MS Thesis, Air Force Institute of Technology.
27. Morton, S.A. Private communication concerning determination of Jacobian elements by numerical scheme, August 1993.
28. National Advisory Committee for Aeronautics. *Equations, Tables, and Charts for Compressible Flow*. Report 1135. Ames Research Staff.
29. Peake, D.J., Fischer, D.F., and McRae, D.S. 1982 Flight, Wind Tunnel, and Numerical Experiments with a Slender Cone at Incidence. *AIAA Journal*, **20** (10), 1338.
30. Peake, D.J., and Tobak, M. 1982 Three-Dimensional Flows About Simple Components at Angle of Attack. *AGARD Report LS-121*, No. 2.
31. Peyret, R. and Taylor, T.D. 1983 *Computational Methods for Fluid Flow*. Springer-Verlag, New York.
32. Siclari, M.J. 1992 Asymmetric Separated Flows at Supersonic Speeds. *AIAA Journal*, **30** (1), 124.
33. Siclari, M.J., and Marconi, F. 1991 Computation of Navier-Stokes Solutions Exhibiting Asymmetric Vortices. *AIAA Journal*, **29** (1), 32.
34. Stahl, W.H., Mahmood, M., and Asghar, A. 1992 Experimental Investigations of the Vortex Flow on Delta Wings at High Incidence. *AIAA Journal*, **30** (4), 1027.
35. Thompson, J.F. 1985 *Numerical Grid Generation*. North-Holland, New York.
36. Vanden, K., and Belk, D. 1991 Numerical Investigation of Subsonic and Supersonic Asymmetric Vortical Flow. *AIAA Paper 91-2869*.
37. White, F.M. 1991 *Viscous Fluid Flow*. McGraw-Hill, New York.
38. Yanta, W.J., and Wardlaw, A.B. 1982 The Secondary Separation Region on a Body at High Angles of Attack. *AIAA Paper 82-0343*.
39. Zilliac, G.G., Degani, D., and Tobak, M. 1991 Asymmetric Vortices on a Slender Body of Revolution. *AIAA Journal*, **29** (5), 667.

Appendix A. Derivation of Governing Equations

The derivation of the non-dimensional governing equations begins with the dimensional Navier-Stokes equations of motion for a compressible fluid in spherical coordinates, as found in reference (17). The five governing equations consist of conservation of mass, momentum (three equations), and internal energy:

Continuity equation

$$\frac{\partial \rho}{\partial t} + \frac{1}{r^2} \frac{\partial}{\partial r} (r^2 \rho u) + \frac{1}{r \sin \theta} \frac{\partial}{\partial \theta} (\rho v \sin \theta) + \frac{1}{r \sin \theta} \frac{\partial}{\partial \phi} (\rho w) = 0 \quad (\text{A.1})$$

r momentum equation

$$\begin{aligned} \rho \left[\frac{Du}{Dt} - \frac{v^2 + w^2}{r} \right] &= F_r - \frac{\partial P}{\partial r} + \frac{\partial}{\partial r} \left[2\mu \frac{\partial u}{\partial r} + \lambda \nabla \cdot \mathbf{V} \right] + \frac{1}{r} \frac{\partial}{\partial \theta} \left[\mu \left\{ r \frac{\partial}{\partial r} \left(\frac{v}{r} \right) + \frac{1}{r} \frac{\partial u}{\partial \theta} \right\} \right] \\ &+ \frac{1}{r \sin \theta} \frac{\partial}{\partial \phi} \left[\mu \left\{ \frac{1}{r \sin \theta} \frac{\partial u}{\partial \phi} + r \frac{\partial}{\partial r} \left(\frac{w}{r} \right) \right\} \right] + \frac{\mu}{r} \left[4 \frac{\partial u}{\partial r} - \frac{2}{r} \frac{\partial v}{\partial \theta} - \frac{4u}{r} \right. \\ &\left. - \frac{2}{r \sin \theta} \frac{\partial w}{\partial \phi} - \frac{2v \cot \theta}{r} + r \cot \theta \frac{\partial}{\partial r} \left(\frac{v}{r} \right) + \frac{\cot \theta}{r} \frac{\partial u}{\partial \theta} \right] \end{aligned} \quad (\text{A.2})$$

θ -momentum equation

$$\begin{aligned} \rho \left[\frac{Dv}{Dt} + \frac{uv}{r} - \frac{w^2 \cot \theta}{r} \right] &= F_\theta - \frac{1}{r} \frac{\partial P}{\partial \theta} + \frac{1}{r} \frac{\partial}{\partial \theta} \left[\frac{2\mu}{r} \left(\frac{\partial v}{\partial \theta} + u \right) + \lambda \nabla \cdot \mathbf{V} \right] \\ &+ \frac{1}{r \sin \theta} \frac{\partial}{\partial \phi} \left[\mu \left\{ \frac{\sin \theta}{r} \frac{\partial}{\partial \theta} \left(\frac{w}{\sin \theta} \right) + \frac{1}{r \sin \theta} \frac{\partial v}{\partial \phi} \right\} \right] + \frac{\partial}{\partial r} \left[\mu \left\{ r \frac{\partial}{\partial r} \left(\frac{v}{r} \right) + \frac{1}{r} \frac{\partial u}{\partial \theta} \right\} \right] \\ &+ \frac{\mu}{r} \left[2 \left(\frac{1}{r} \frac{\partial v}{\partial \theta} - \frac{1}{r \sin \theta} \frac{\partial w}{\partial \phi} - \frac{v \cot \theta}{r} \right) \cot \theta + 3 \left\{ r \frac{\partial}{\partial r} \left(\frac{v}{r} \right) + \frac{1}{r} \frac{\partial u}{\partial \theta} \right\} \right] \end{aligned} \quad (\text{A.3})$$

ϕ -momentum equation

$$\begin{aligned} \rho \left[\frac{Dw}{Dt} + \frac{wu}{r} + \frac{vw \cot \theta}{r} \right] &= F_\phi - \frac{1}{r \sin \theta} \frac{\partial P}{\partial \phi} \\ &+ \frac{1}{r \sin \theta} \frac{\partial}{\partial \phi} \left[\frac{2\mu}{r} \left(\frac{1}{\sin \theta} \frac{\partial w}{\partial \phi} + u + v \cot \theta \right) + \lambda \nabla \cdot \mathbf{V} \right] \\ &+ \frac{\partial}{\partial r} \left[\mu \left\{ \frac{1}{r \sin \theta} \frac{\partial u}{\partial \phi} + r \frac{\partial}{\partial r} \left(\frac{w}{r} \right) \right\} \right] + \frac{1}{r} \frac{\partial}{\partial \theta} \left[\mu \left\{ \frac{\sin \theta}{r} \frac{\partial}{\partial \theta} \left(\frac{w}{\sin \theta} \right) + \frac{1}{r \sin \theta} \frac{\partial v}{\partial \phi} \right\} \right] \end{aligned}$$

$$+ \frac{\mu}{r} \left[3 \left\{ \frac{1}{r \sin \theta} \frac{\partial u}{\partial \phi} + r \frac{\partial}{\partial r} \left(\frac{w}{r} \right) \right\} + 2 \cot \theta \left\{ \frac{\sin \theta}{r} \frac{\partial}{\partial \theta} \left(\frac{w}{\sin \theta} \right) + \frac{1}{r \sin \theta} \frac{\partial v}{\partial \phi} \right\} \right] \quad (\text{A.4})$$

Energy equation

$$\begin{aligned} \rho \frac{De}{Dt} + P \nabla \cdot \mathbf{V} &= \frac{\partial Q}{\partial t} + \Phi + \frac{1}{r^2} \frac{\partial}{\partial r} \left(r^2 \kappa \frac{\partial T}{\partial r} \right) \\ &+ \frac{1}{r^2 \sin \theta} \frac{\partial}{\partial \theta} \left(\kappa \sin \theta \frac{\partial T}{\partial \theta} \right) + \frac{1}{r^2 \sin^2 \theta} \frac{\partial}{\partial \phi} \left(\kappa \frac{\partial T}{\partial \phi} \right) - \nabla \cdot \mathbf{q}_r \end{aligned} \quad (\text{A.5})$$

where \mathbf{q}_r is the radiation heat flux vector and is assumed to be zero. Q represents internal heat generation and is also assumed to be zero. The body forces F_r, F_θ, F_ϕ are assumed negligible and so are discarded. Φ is the viscous dissipation function:

$$\begin{aligned} \Phi &= \mu \left[2 \left\{ \left(\frac{\partial u}{\partial r} \right)^2 + \left(\frac{1}{r \sin \theta} \frac{\partial w}{\partial \phi} + \frac{u}{r} + \frac{v \cot \theta}{r} \right)^2 \right. \right. \\ &\quad \left. \left. \left(\frac{1}{r} \frac{\partial v}{\partial \theta} + \frac{u}{r} \right)^2 \right\} + \left\{ \frac{1}{r \sin \theta} \frac{\partial v}{\partial \phi} + \frac{\sin \theta}{r} \frac{\partial}{\partial \theta} \left(\frac{w}{\sin \theta} \right) \right\}^2 \right. \\ &\quad \left. \left\{ \frac{1}{r \sin \theta} \frac{\partial u}{\partial \phi} + r \frac{\partial}{\partial r} \left(\frac{w}{r} \right) \right\}^2 + \left\{ r \frac{\partial}{\partial r} \left(\frac{v}{r} \right) + \frac{1}{r} \frac{\partial u}{\partial \theta} \right\}^2 \right] \\ &+ \lambda \left[\frac{\partial u}{\partial r} + \frac{1}{r} \frac{\partial v}{\partial \theta} + \frac{2u}{r} + \frac{1}{r \sin \theta} \frac{\partial w}{\partial \phi} + \frac{v \cot \theta}{r} \right]^2. \end{aligned} \quad (\text{A.6})$$

The material derivative in spherical coordinates is defined as

$$\frac{D}{Dt} \equiv \frac{\partial}{\partial t} + u \frac{\partial}{\partial r} + \frac{v}{r} \frac{\partial}{\partial \theta} + \frac{w}{r \sin \theta} \frac{\partial}{\partial \phi}, \quad (\text{A.7})$$

and the divergence operation in spherical coordinates is

$$\nabla \cdot \mathbf{V} = \frac{1}{r^2} \frac{\partial}{\partial r} (r^2 u) + \frac{1}{r \sin \theta} \frac{\partial}{\partial \theta} (v \sin \theta) + \frac{1}{r \sin \theta} \frac{\partial w}{\partial \phi}, \quad (\text{A.8})$$

where \mathbf{V} is the velocity vector. Two of the major assumptions in this study are steady-state flow and conical similarity. Steady state implies $\frac{\partial f}{\partial t} = 0$ and conical similarity implies $\frac{\partial f}{\partial r} = 0$, where f is one of the dependent variables. The pressure, P , is written in terms of the density, ρ , and the internal energy, e , assuming a thermally and calorically perfect gas, by

$$P = \rho RT \quad e = c_v T. \quad (\text{A.9})$$

Elimination of T from (A.9) yields

$$P = \frac{eR\rho}{c_v} \quad (\text{A.10})$$

Using

$$\frac{R}{c_v} = \frac{c_p - c_v}{c_v} = \gamma - 1, \quad (\text{A.11})$$

pressure is written as

$$P = (\gamma - 1)\rho e. \quad (\text{A.12})$$

The temperature, T , is written in terms of e using equation (A.10). Stokes' hypothesis is also used, $\lambda = -\frac{2}{3}\mu$. The equations, after all terms are expanded and the above relationships implemented, are then non-dimensionalized. The dependent and independent variables are non-dimensionalized as follows:

$$\begin{aligned} \rho^* &= \frac{\rho}{\rho_\infty} & r^* &= \frac{P}{\rho_\infty U_\infty^2} & r^* &= \frac{r}{L} \\ u^* &= \frac{u}{U_\infty} & v^* &= \frac{v}{U_\infty} & w^* &= \frac{w}{U_\infty} \\ e^* &= \frac{e}{U_\infty^2} & T^* &= \frac{T}{T_\infty} & \mu^* &= \frac{\mu}{\mu_\infty} \end{aligned}$$

The coordinate directions θ and ϕ are already non-dimensional angles, so they are not affected in this process. The non-dimensional viscosity is replaced with the linear relationship $\mu = \hat{c}_1 e + \hat{c}_2$, developed in Chapter 2, providing the final form of the non-dimensional equations (after dropping the (*) for convenience):

Continuity equation

$$2\rho u \sin\theta + \rho v \cos\theta + v\rho_\theta \sin\theta + \rho v_\theta \sin\theta + \rho w_\phi + w\rho_\phi = 0 \quad (\text{A.13})$$

r-momentum equation

$$\begin{aligned} \rho r \left[v u_\theta + \frac{w u_\phi}{\sin\theta} - v^2 - w^2 \right] + \frac{\hat{c}_1 e_\theta}{Re} [v - u_\theta] + \frac{\hat{c}_1 e_\phi}{Re} \left[\frac{w}{\sin\theta} - \frac{u_\phi}{\sin^2\theta} \right] \\ + \frac{\hat{c}_1 e + \hat{c}_2}{Re} \left[\frac{8u}{3} + \frac{7v \cot\theta}{3} + \frac{7v_\theta}{3} + \frac{7w_\phi}{3 \sin\theta} - u_{\theta\theta} - \frac{u_{\phi\phi}}{\sin^2\theta} - u_\theta \cot\theta \right] = 0 \quad (\text{A.14}) \end{aligned}$$

θ -momentum equation

$$\begin{aligned}
 & \rho r \left[vv_\theta + \frac{wv_\phi}{\sin\theta} + uv - w^2 \cot\theta \right] + r(\gamma - 1) [\rho e_\theta + e\rho_\theta] \\
 & + \frac{\hat{c}_1 e_\theta}{Re} \left[\frac{2v \cot\theta}{3} + \frac{2w_\phi}{3 \sin\theta} - \frac{4v_\theta}{3} - \frac{2u}{3} \right] + \frac{\hat{c}_1 e_\phi}{Re} \left[\frac{w \cos\theta}{\sin^2\theta} - \frac{w_\theta}{\sin\theta} - \frac{v_\phi}{\sin^2\theta} \right] \\
 & + \frac{\hat{c}_1 e + \hat{c}_2}{Re} \left[2v + \frac{7w_\phi \cos\theta}{3 \sin^2\theta} + 2v \cot^2\theta - \frac{4v_{\theta\theta}}{3} - \frac{v_{\phi\phi}}{\sin^2\theta} \right. \\
 & \quad \left. - \frac{w_{\theta\phi}}{3 \sin\theta} - \frac{8u_\theta}{3} - \frac{4v_\theta \cot\theta}{3} - \frac{2v}{3 \sin^2\theta} \right] = 0
 \end{aligned} \tag{A.15}$$

ϕ -momentum equation

$$\begin{aligned}
 & \rho r \left[vw_\theta + \frac{ww_\phi}{\sin\theta} + wu + vw \cot\theta \right] + \frac{r(\gamma - 1)}{\sin\theta} [e\rho_\phi + \rho e_\phi] \\
 & - \frac{\hat{c}_1 e_\theta}{Re} \left[w_\theta - w \cot\theta + \frac{v_\phi}{\sin\theta} \right] - \frac{\hat{c}_1 e_\phi}{Re} \left[\frac{4w_\phi}{3 \sin^2\theta} + \frac{2u}{3 \sin\theta} + \frac{4v \cos\theta}{3 \sin^2\theta} - \frac{2v_\theta}{3 \sin\theta} \right] \\
 & - \frac{\hat{c}_1 e + \hat{c}_2}{Re} \left[\frac{4w_{\phi\phi}}{3 \sin^2\theta} + w_{\theta\theta} + \frac{v_{\theta\phi}}{3 \sin\theta} + \frac{8u_\phi}{3 \sin\theta} + \frac{7v_\phi \cos\theta}{3 \sin^2\theta} \right. \\
 & \quad \left. - 2w + \frac{w}{\sin^2\theta} + w_\theta \cot\theta - 2w \cot^2\theta \right] = 0
 \end{aligned} \tag{A.16}$$

Energy equation

$$\begin{aligned}
 & \rho r \left[ve_\theta + \frac{we_\phi}{\sin\theta} \right] + (\gamma - 1) r e \rho \left[2u + v \cot\theta + v_\theta + \frac{w_\phi}{\sin\theta} \right] \\
 & - \frac{\gamma(\hat{c}_1 e + \hat{c}_2)}{Pr Re} \left[e_\theta \cot\theta + e_{\theta\theta} + \frac{e_{\phi\phi}}{\sin^2\theta} \right] - \frac{\gamma \hat{c}_1}{Pr Re} \left[e_\theta^2 + \frac{e_\phi^2}{\sin^2\theta} \right] \\
 & - \frac{\hat{c}_1 e + \hat{c}_2}{Re} \left[\frac{4v_\theta^2}{3} + \frac{4uv_\theta}{3} + \frac{4u^2}{3} + \frac{4w_\phi^2}{3 \sin^2\theta} + \frac{4v^2 \cot^2\theta}{3} \right. \\
 & \quad + \frac{4uw_\phi}{3 \sin\theta} + \frac{8vw_\phi \cot\theta}{3 \sin\theta} + \frac{4uv \cot\theta}{3} + \frac{v_\phi^2}{\sin^2\theta} + w_\theta^2 + w^2 \cot^2\theta \\
 & \quad \left. + \frac{2w_\theta v_\phi}{\sin\theta} - \frac{2wv_\phi \cot\theta}{\sin\theta} - 2ww_\theta \cot\theta + \frac{u_\phi^2}{\sin^2\theta} - \frac{2wu_\phi}{\sin\theta} \right]
 \end{aligned}$$

$$+w^2 + v^2 + u_\theta^2 - 2vu_\theta - \frac{4v_\theta w_\phi}{3 \sin\theta} - \frac{4vv_\theta \cot\theta}{3} \Big] = 0 \quad (\text{A.17})$$

To check to accuracy of the preceeding derivation, the continuity and momentum equations were re-derived using the non-dimensional Navier-Stokes equations found in Reference (31). The continuity equation is

$$\frac{\partial \rho}{\partial t} + \frac{1}{h_1 h_2 h_3} \frac{\partial}{\partial x_j} \left(\frac{1}{h_j} h_1 h_2 h_3 \rho u_j \right) = 0. \quad (\text{A.18})$$

The momentum equations for the x_1 , x_2 , and x_3 coordinate directions are, respectively,

$$\begin{aligned} \frac{\partial}{\partial t}(\rho u_1) + \frac{1}{h_1 h_2 h_3} \frac{\partial}{\partial x_j} \left(\frac{1}{h_j} h_1 h_2 h_3 \mathcal{T}_{j1} \right) + \frac{1}{h_1 h_2} \left(\mathcal{T}_{12} \frac{\partial h_1}{\partial x_2} - \mathcal{T}_{22} \frac{\partial h_2}{\partial x_1} \right) \\ + \frac{1}{h_1 h_3} \left(\mathcal{T}_{13} \frac{\partial h_1}{\partial x_3} - \mathcal{T}_{33} \frac{\partial h_3}{\partial x_1} \right) = 0, \end{aligned} \quad (\text{A.19})$$

$$\begin{aligned} \frac{\partial}{\partial t}(\rho u_2) + \frac{1}{h_1 h_2 h_3} \frac{\partial}{\partial x_j} \left(\frac{1}{h_j} h_1 h_2 h_3 \mathcal{T}_{j2} \right) + \frac{1}{h_2 h_3} \left(\mathcal{T}_{23} \frac{\partial h_2}{\partial x_3} - \mathcal{T}_{33} \frac{\partial h_3}{\partial x_2} \right) \\ + \frac{1}{h_2 h_1} \left(\mathcal{T}_{21} \frac{\partial h_2}{\partial x_1} - \mathcal{T}_{11} \frac{\partial h_1}{\partial x_2} \right) = 0, \end{aligned} \quad (\text{A.20})$$

$$\begin{aligned} \frac{\partial}{\partial t}(\rho u_3) + \frac{1}{h_1 h_2 h_3} \frac{\partial}{\partial x_j} \left(\frac{1}{h_j} h_1 h_2 h_3 \mathcal{T}_{j3} \right) + \frac{1}{h_3 h_1} \left(\mathcal{T}_{31} \frac{\partial h_3}{\partial x_1} - \mathcal{T}_{11} \frac{\partial h_1}{\partial x_3} \right) \\ + \frac{1}{h_2 h_1} \left(\mathcal{T}_{32} \frac{\partial h_3}{\partial x_2} - \mathcal{T}_{22} \frac{\partial h_2}{\partial x_3} \right) = 0. \end{aligned} \quad (\text{A.21})$$

The components of the tensor \mathcal{T} , \mathcal{T}_{ij} , are given by

$$\mathcal{T}_{ij} = \rho u_i u_j + P \delta_{ij} - \frac{1}{Re} \tau_{ij}, \quad (\text{A.22})$$

where

$$\tau_{ij} = \lambda (\nabla \cdot \mathbf{V}) \delta_{ij} + 2\mu (\text{def} \mathbf{V})_{ij} \quad (\text{A.23})$$

$$\nabla \cdot \mathbf{V} = \frac{1}{h_1 h_2 h_3} \frac{\partial}{\partial x_i} \left(\frac{1}{h_i} h_1 h_2 h_3 u_i \right) \quad (\text{A.24})$$

$$(\text{def} \mathbf{V})_{11} = \frac{1}{h_1} \left(\frac{\partial u_1}{\partial x_1} + \frac{u_2}{h_2} \frac{\partial h_1}{\partial x_2} + \frac{u_3}{h_3} \frac{\partial h_1}{\partial x_3} \right) \quad (\text{A.25})$$

$$(defV)_{22} = \frac{1}{h_2} \left(\frac{\partial u_2}{\partial x_2} + \frac{u_3}{h_3} \frac{\partial h_2}{\partial x_3} + \frac{u_1}{h_1} \frac{\partial h_2}{\partial x_1} \right) \quad (A.26)$$

$$(defV)_{33} = \frac{1}{h_3} \left(\frac{\partial u_3}{\partial x_3} + \frac{u_1}{h_1} \frac{\partial h_3}{\partial x_1} + \frac{u_2}{h_2} \frac{\partial h_3}{\partial x_2} \right) \quad (A.27)$$

$$(defV)_{ij(i \neq j)} = \frac{1}{2} \left[\frac{1}{h_i} \frac{\partial u_j}{\partial x_i} + \frac{1}{h_j} \frac{\partial u_i}{\partial x_j} - \frac{1}{h_i h_j} \left(u_i \frac{\partial h_i}{\partial x_j} + u_j \frac{\partial h_j}{\partial x_i} \right) \right], \quad (A.28)$$

and δ_{ij} is the Kronecker delta. For a spherical coordinate system,

$$\begin{aligned} h_1 &= 1 & x_1 &= r & u_1 &= u \\ h_2 &= r & x_2 &= \theta & u_2 &= v \\ h_3 &= r \sin \theta & x_3 &= \phi & u_3 &= w. \end{aligned}$$

When equations (A.19 - A.22) are expanded and the continuity equation (A.19) subtracted out of the momentum equations, the results are the same as the previous derivation for (A.15 - A.17). The energy equation was not checked through an alternate derivation.

Appendix B. Derivation of Analytical Jacobian Elements

As an example of how all the equations are manipulated, the continuity equation will be transformed from (ϕ, θ) physical space to (ξ, η) computational space and the analytical Jacobian elements derived. The other four equations are then handled in the same manner to determine their respective Jacobian elements.

With the subscripts θ and ϕ representing differentiation, the non-dimensional continuity equation in spherical coordinates, as developed in Appendix A, becomes

$$2\rho u \sin\theta + \rho v \cos\theta + v\rho_\theta \sin\theta + \rho v_\theta \sin\theta + \rho w_\phi + w\rho_\phi = 0.$$

The derivatives, transformed using the relationships outlined in Chapter 2, are

$$\rho_\phi = \xi_\phi \rho_\xi + \eta_\phi \rho_\eta, \quad \rho_\theta = \xi_\theta \rho_\xi + \eta_\theta \rho_\eta$$

$$v_\theta = \xi_\theta v_\xi + \eta_\theta v_\eta, \quad w_\phi = \xi_\phi w_\xi + \eta_\phi w_\eta.$$

The ξ and η derivatives are now expressed in terms of the nine-point stencil, shown in Figure 2.4, using central differences about node k . The central differences needed for the continuity equation are

$$\rho_\xi \approx \frac{\rho_{ke} - \rho_{kw}}{2\Delta\xi} \quad \rho_\eta \approx \frac{\rho_{kn} - \rho_{ks}}{2\Delta\eta} \quad (\text{B.1})$$

$$v_\xi \approx \frac{v_{ke} - v_{kw}}{2\Delta\xi} \quad v_\eta \approx \frac{v_{kn} - v_{ks}}{2\Delta\eta} \quad (\text{B.2})$$

$$w_\xi \approx \frac{w_{ke} - w_{kw}}{2\Delta\xi} \quad w_\eta \approx \frac{w_{kn} - w_{ks}}{2\Delta\eta}. \quad (\text{B.3})$$

Approximations (B.1 – B.3) are second-order-accurate in the node spacing. Using a square computational cell, $\Delta\xi = \Delta\eta = 1$, the continuity equation becomes

$$F \equiv 2\rho_k u_k \sin\theta + \rho_k v_k \cos\theta + \frac{v_k \sin\theta}{2} [\xi_\theta(\rho_{ke} - \rho_{kw}) + \eta_\theta(\rho_{kn} - \rho_{ks})] \\ + \frac{\rho_k \sin\theta}{2} [\xi_\theta(v_{ke} - v_{kw}) + \eta_\theta(v_{kn} - v_{ks})]$$

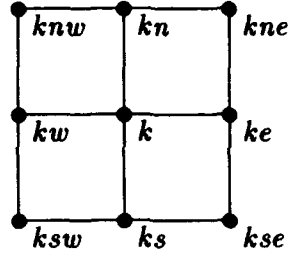


Figure B.1 Nine-point Stencil for interior nodes

$$\begin{aligned}
 & + \frac{\rho_k}{2} [\xi_\phi(w_{ke} - w_{kw}) + \eta_\phi(w_{kn} - w_{ks})] \\
 & + \frac{w_k}{2} [\xi_\phi(\rho_{ke} - \rho_{kw}) + \eta_\phi(\rho_{kn} - \rho_{ks})] = 0.
 \end{aligned} \tag{B.4}$$

The analytical Jacobian elements are now determined by taking partial derivatives of (B.4) with respect to each of the discrete flow variables in the nine-point stencil, shown in Figure B.1. The Jacobian elements for the continuity equation are found to be

$$\begin{aligned}
 \frac{\partial F}{\partial \rho_k} &= 2u_k \sin\theta + v_k \cos\theta + \frac{\sin\theta}{2} [\xi_\theta(v_{ke} - v_{kw}) + \eta_\theta(v_{kn} - v_{ks})] \\
 & + \frac{1}{2} [\xi_\phi(w_{ke} - w_{kw}) + \eta_\phi(w_{kn} - w_{ks})],
 \end{aligned}$$

$$\frac{\partial F}{\partial \rho_{ke}} = \frac{v_k \xi_\theta \sin\theta}{2} + \frac{w_k \xi_\phi}{2}, \quad \frac{\partial F}{\partial \rho_{kw}} = -\frac{\partial F}{\partial \rho_{ke}},$$

$$\frac{\partial F}{\partial \rho_{kn}} = \frac{v_k \eta_\theta \sin\theta}{2} + \frac{w_k \eta_\phi}{2}, \quad \frac{\partial F}{\partial \rho_{ks}} = -\frac{\partial F}{\partial \rho_{kn}},$$

$$\frac{\partial F}{\partial u_k} = 2\rho_k \sin\theta,$$

$$\frac{\partial F}{\partial v_k} = \rho_k \cos\theta + \frac{\sin\theta}{2} [\xi_\theta(\rho_{ke} - \rho_{kw}) + \eta_\theta(\rho_{kn} - \rho_{ks})],$$

$$\frac{\partial F}{\partial v_{ke}} = \frac{\rho_k \xi_\theta \sin\theta}{2}, \quad \frac{\partial F}{\partial v_{kw}} = -\frac{\partial F}{\partial v_{ke}},$$

$$\frac{\partial F}{\partial v_{kn}} = \frac{\rho_k \eta_\theta \sin \theta}{2}, \quad \frac{\partial F}{\partial v_{ks}} = -\frac{\partial F}{\partial v_{kn}},$$

$$\frac{\partial F}{\partial w_k} = \frac{1}{2} [\xi_\phi (\rho_{kc} - \rho_{kw}) + \eta_\phi (\rho_{kn} - \rho_{ks})],$$

$$\frac{\partial F}{\partial w_{kc}} = \frac{\rho_k \xi_\phi}{2}, \quad \frac{\partial F}{\partial w_{kw}} = -\frac{\partial F}{\partial w_{kc}},$$

$$\frac{\partial F}{\partial w_{kn}} = \frac{\rho_k \eta_\phi}{2}, \quad \frac{\partial F}{\partial w_{ks}} = -\frac{\partial F}{\partial w_{kn}}.$$

Vita

PII Redacted

Captain Larry K. Waters [REDACTED]. He graduated from Gull Lake High School in Richland, Michigan in 1978 and enlisted in the United States Air Force on 4 May 1979. After serving as a computer operator and programmer for six years, he was selected for the Airman Educational Commissioning Program (AECP). He attended the University of Missouri-Rolla, where he graduated with a Bachelor of Science in Aerospace Engineering in May 1988. He then attended Officer Training School at Lackland AFB, Texas, where he was selected as First Honor Graduate for class 88-12, for which he was awarded a regular commission. He then served four years at the Phillips Laboratory, Kirtland AFB, New Mexico, where he worked on a variety of high energy laser projects, until entering the School of Engineering, Air Force Institute of Technology, in May 1992.

[REDACTED] [REDACTED]

REPORT DOCUMENTATION PAGE

Form Approved
OMB No. 0704-0188

Public reporting burden for this collection of information is estimated to average 1 hour per response, including the time for reviewing instructions, searching existing data sources, gathering and maintaining the data needed, and completing and reviewing the collection of information. Send comments regarding this burden estimate or any other aspect of this collection of information, including suggestions for reducing this burden, to Washington Headquarters Services, Directorate for Information Operations and Reports, 1215 Jefferson Davis Highway, Suite 1204, Arlington, VA 22202-4302, and to the Office of Management and Budget, Paperwork Reduction Project (0704-0188), Washington, DC 20503.

1. AGENCY USE ONLY (Leave blank)		2. REPORT DATE December 1993	3. REPORT TYPE AND DATES COVERED Master's Thesis	
4. TITLE AND SUBTITLE A NUMERICAL DETERMINATION OF BIFURCATION POINTS FOR LOW REYNOLDS NUMBER CONICAL FLOWS			5. FUNDING NUMBERS	
6. AUTHOR(S) Larry K. Waters, Captain, USAF				
7. PERFORMING ORGANIZATION NAME(S) AND ADDRESS(ES) Air Force Institute of Technology, WPAFB OH 45433-6583			8. PERFORMING ORGANIZATION REPORT NUMBER AFTT/GAE/ENY/93D-29	
9. SPONSORING/MONITORING AGENCY NAME(S) AND ADDRESS(ES) Dr D. Belk Wright Laboratory, Armament Directorate Eglin AFB, Florida 32542			10. SPONSORING/MONITORING AGENCY REPORT NUMBER	
11. SUPPLEMENTARY NOTES				
12a. DISTRIBUTION/AVAILABILITY STATEMENT Approved for public release; distribution unlimited			12b. DISTRIBUTION CODE	
13. ABSTRACT (Maximum 200 words) It has long been established that supersonic flow over axisymmetric conical bodies at high angles of attack tend to develop a side force due to vortical asymmetry. One of the proposed reasons for the asymmetry is a bifurcation point in the solution of the Navier-Stokes equations. This study investigated the possible existence of a bifurcation point in the Navier-Stokes equations for subsonic laminar flow. Newton's method, with gauss elimination, was used to solve the steady-state, viscous, compressible Navier-Stokes equations in spherical coordinates assuming conical similarity.				
14. SUBJECT TERMS Navier-Stokes, Viscous, Vortical Flow, Bifurcation, Newton's Method			15. NUMBER OF PAGES 75	
			16. PRICE CODE	
17. SECURITY CLASSIFICATION OF REPORT Unclassified	18. SECURITY CLASSIFICATION OF THIS PAGE Unclassified	19. SECURITY CLASSIFICATION OF ABSTRACT Unclassified	20. LIMITATION OF ABSTRACT UL	